Chapter 2

Comparison of biodegradable polymer with polyethylene at the macroscopic and molecular scale in response to mechanical and thermal perturbations

2.1 Introduction

The mass usage of petroleum-based polymers which are non-bio-based and non-biodegradable polymers has led to unprecedented damage to the earth in the form of plastic and micro-plastic pollution and energy crisis due to the heavy release of carbon dioxide (CO_2) into atmosphere [1, 2, 3, 4]. To meet the energy crisis scientists across the globe have been working effectively to develop polymers that are synthesized from natural sources, like bio-polyethylene, bio-polypropylene, etc., and are strong enough to compete with traditional petroleum-based polymers, but there is still some amount of environmental damage during degradation of these polymers [5, 6, 7]. In such a scenario, biodegradable polymers which are derived from renewable resources like starch [8, 9, 10] or synthesized, like polyglycolic acid (PGA), polylactic acid (PLA) [11, 12, 13], or produced from micro-organisms (poly hydroxybutyrate or poly hydroxy alkanoate) are becoming an effective alternative to the traditional non-biodegradable polymers. Several technological advances have led recently to the usage of biodegradable polymers in the food storage and processing

industry and packaging [8, 9]. PLA and starch-based plastics have been successful in becoming an alternative to the synthetic plastics used in food packaging [11]. Apart from food packaging, a major challenge to biodegradable plastics is their industrial applications which require higher mechanical strength which is comparable to petroleum-based polymers like polyethylene.

Polypropylene carbonate (PPC) is a biodegradable polymer that is synthesized by copolymerization of propylene oxide with carbon dioxide and has drawn much attention in both research and industrial fields [14, 15]. PPC has been used in packaging materials, adhesives, solar cells, and biomedical materials [4]. The good biodegradability of PPC in both soil and buffer solutions attract its utilization in packaging materials [16]. Also, the production of PPC uses CO_2 which not only reduced the greenhouse effect but also alleviates the energy crisis. But the low degradation temperature and low glass transition temperature of PPC limits its applications for which melt blending of PPC with other biodegradable polymers like starch and poly butyrate succinate (PBS) have been studied which led to a limited improvement in thermal properties [17, 18, 19]. Moreover, the molten state of these polymers possesses a semi-fluid-like flow behavior. If the molten state is cooled fast enough below the glass transition temperature (T_g), it drives the polymer into an unstable nonequilibrium state which drives effective molecular relaxation in the polymer. In this state, the polymer possesses higher configurational entropy as compared to the stable equilibrium state and the polymer starts to achieve a metastable state through a slow structural relaxation phenomenon called physical aging of the polymer. Physical aging, whereby properties evolve as a function of time, changes mechanical and other properties which can have far-reaching consequences in material design and usage [20, 21, 22]. Structural relaxation is a direct consequence of aging which affects the fabrication, designing, and manufacturing of products [23].

Structural relaxations involve changes in the microstructure of polymer which consequently affects the macroscopic properties. Therefore, it is important to investigate the mechanisms that drive the microscopic changes during the aging of a polymer. So far, many studies have concentrated on the free volume changes during annealing and the microscopic relaxation processes along with the effect on macroscopic mechanical, thermal and dielectric properties of amorphous polymers. Particular interests have been shown in the

study of deformation like elastic and plastic responses with annealing which showed remarkable increases in elastic modulus and yield stress in polymeric materials. Investigating the relationship between the large deformation and the structural state of polymers via experiments and atomistic simulations has been beneficial for the polymer industry [24, 25, 26]. Plastic deformation in polymers is widely known to be controlled by chain rearrangements when subjected to excessive loads [27]. Alterations in free volume content affecting the micro and macro mechanical properties upon annealing have been found in glassy polymers like poly(methyl methacrylate) and polycarbonate which support the theory that micro-scale variations can affect the macroscopic mechanical properties of the polymers [23].

Although physical aging and annealing in polymers and their effect on macroscopic properties have been widely studied a deeper insight into the molecular mobility upon thermal treatment and the correlation between the micro-structure and macroscopic mechanical properties is seldom presented. In this chapter, the mechanical response of amorphous and semi-crystalline polymers: polypropylene carbonate (PPC), high-density polyethylene (HDPE), and linear low-density polyethylene (LLDPE) have been studied and their plastic deformation in critically examined. The plastic deformation of the semi-crystalline polymer showed craze formation and cavitation along the direction of tensile forces. The effect of thermal treatment on the polymer near and above T_g has also been studied using Raman spectroscopy. This revealed aging-induced changes in molecular mobility in the polymers. A correlation between the macroscopic mechanical response and molecular scale thermal response has been analyzed to identify the micro-macro relationship in the polymer both in the glassy and non-glassy regime. These studies can be beneficial for the industrial applications of the biodegradable polymers.

2.2 Preparation of polymer films

High-density polyethylene (HDPE) and linear low-density polyethylene (LLDPE) films were obtained from Oil and Natural Gas Corporation, India in the form of sheets of 100 μm thickness which were used without further processing. Polypropylene carbonate (PPC) of molecular weight 50,000 g/mol was purchased from Sigma Aldrich and was used to prepare films without any

further processing. For PPC film preparation, 20% of PPC by weight was dissolved in dichloromethane (purchased from LOBA Chemie) such as to prepare a 10 ml solution. The solution was stirred continuously on a magnetic stirrer at room temperature (27 °C) for 60 minutes. The solution was then casted in the form of a film on a glass substrate which was thoroughly cleaned with chromic acid and dried at room temperature. The casted films were left to dry at room temperature for at least 24 hours before the experiments. Drop casted HDPE films were prepared by using HDPE (molecular weight 1,25,000 g/mol) purchased from Alfa Aesar was used without further processing. 20% of HDPE by weight was dissolved in xylene (purchased from LOBA Chemie) such as to prepare a 10 ml solution. The solution was then stirred continuously with heating up to 60 °C to dissolve HDPE for 30 minutes followed by continuous stirring at room temperature for 30 minutes on a magnetic stirrer. After 60 minutes the solution was cast on a glass substrate and left to dry at room temperature for 24 hours before performing the experiments.

For tensile experiments, the HDPE and LLDPE films were cut from the sheets (obtained from Oil and Natural gas Corporation, India) into strips of 10 cm x 2.5 cm dimension following the ASTM D886 standards. The PPC films were peeled off from the glass substrate and were also cut into the dimensions approved by ASTM D886 standards. For Raman experiments, a small part of the film was cut and placed inside the sample holder.

2.3 Tensile testing

The elastic-plastic behavior of materials is frequently described by the stress-strain curves measured in tensile tests. The tensile tests are used to determine material parameters like Young's modulus, tensile strength, yield point, and elongation at break which are used in selecting material and in component designing. In the tensile test, the specimen or sample is lengthened at a constant speed and the change in length also known as the extension($\triangle$ L) is measured along with the force which is required for that extension, or load (F). From these measured quantities, the stress (σ) and strain (γ) are calculated as:

$$\sigma(\triangle L) = \frac{\triangle L}{S_0} \tag{2.1}$$

$$\gamma(\triangle L) = \frac{\triangle L}{L_0} \tag{2.2}$$

where, S_0 is the original cross section of the specimen and L_0 is the original gauge length. The stress-strain curves obtained from tensile tests are different for different materials depending on the characteristics of the materials.

A typical tensile tester also known as a Universal Testing Machine (UTM) consists of a load cell, a cross-head, an extensometer, a specimen grid, and a set of electronics to run the system. The entire system is controlled with software run by the computer. The load cell measures the force required to extend the specimen. The cross-head controls the rate at which the specimen is extended. The specimen is fixed at both the top and bottom ends with the help of the specimen grids. For the present study, a calibrated Mecmesin Multitest-i10 Universal Testing Machine with a 25 N load cell was used. The width of the gauge section was set as 25 mm and the gauge length was 50 mm for all the experiments and the tests were performed at room temperature (25 °C). The experiments were performed with a constant crosshead displacement rate of 100 mm/min. The stress and strain were measured with the help of EmperorTM software which contained predefined test procedures to determine critical parameters.

2.4 Response to mechanical perturbation

The mechanical properties of any material can be determined based on their modulus of elasticity, shear modulus, bulk modulus, or any other microscopic mechanical response like nanoindentation but a very general and ideal way to determine the macroscopic mechanical response is from the stress-strain relationship. The stress-strain response of PPC is shown in Figure 2.1(a), HDPE is shown in Figure 2.1(b) and LLDPE is shown in Figure 2.1(c). The stress-strain response of three sets of samples is represented in different colors in Figure 2.1. The different stress-strain response of polymers is mainly due to the difference in the amount of crystalline/amorphous content present in the polymer and also due to its proximity to glass transition temperature [28]. The stress-strain response of polymer films can be understood by dividing it into two main regions: elastic region (linear region), and plastic deformation region (the

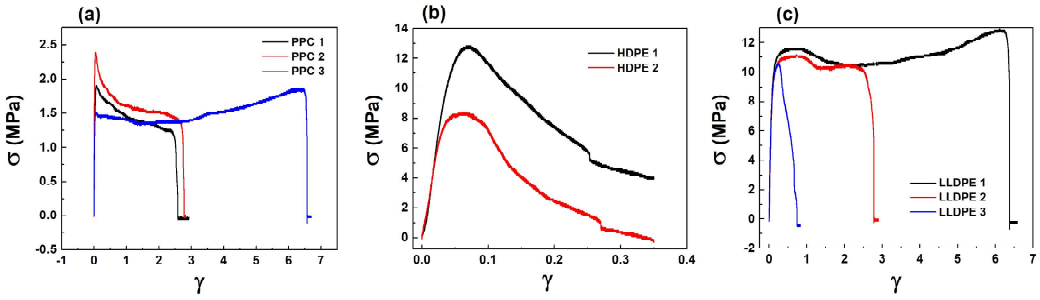

FIGURE 2.1: Stress-strain response of (a) Polypropylene carbonate (PPC), (b) High-density polyethylene (HDPE) and (c) Linear-low density polyethylene (LLDPE) for different sets of polymer films

non-linear region just before the polymer starts yielding). During yielding the stress decreases sharply with a small change in strain and the polymer film breaks.

2.4.1 Elastic response

In an ideal stress-strain curve, the elastic response is represented as a continuous increase in stress with increasing strain. This region represents the elastic character of the polymer and provides information about the elasticity of polymer film. The polymer elasticity is determined by a reversible deformation in the polymer chain molecules, the film extends and the system stores elastic energy which can be released on unloading [28]. The elastic response of PPC, HDPE, and LLDPE films is given in Figure 2.2(a), (b) and (c) respectively. The elasticity can be quantified in terms of Young's modulus and tensile strength of the polymer. The slope of the elastic region gives Young's modulus of the polymer film which is represented as a black solid line in Figure 2.2. The maxima of the elastic region where the stress becomes almost constant with increasing strain give the tensile strength of the polymer film which is represented as a black dashed line in Figure 2.2.

2.4.2 Plastic response

Plastic deformation of polymers plays a crucial role in determining the mechanical properties of polymers. It involves several mechanisms from the crystalline and amorphous content of the polymer. During deformation, the

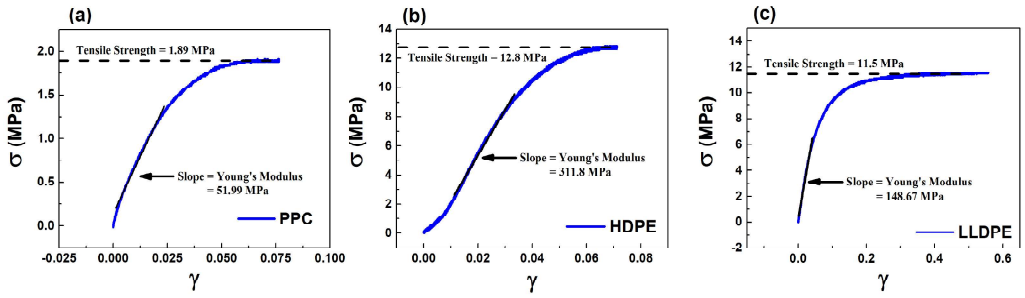

FIGURE 2.2: Elastic response of (a) PPC, (b) HDPE, and (c) LLDPE. the solid black line indicates the slope of the linear region representing Young's modulus of the polymer film and the black dashed line represents the tensile strength of the polymer film

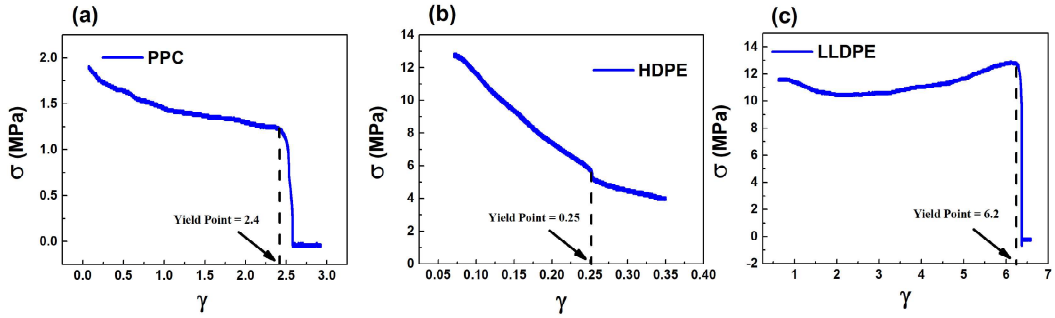

FIGURE 2.3: Plastic deformation region (a) PPC, (b) HDPE, and (c) LLDPE. The black dashed line indicated the yield point of the polymer films.

polymer experiences a variation in its micro-structure which is an important factor that governs the stress-strain response of the polymer. Figure 2.3 represents the plastic deformation region for (a) PPC, (b) HDPE, and (c) LLDPE.

Figure 2.3(a) represents the plastic deformation region of PPC film. With the onset of plastic deformation, a slow decrease in stress is observed from 0.2% strain, at this point, local necking of the polymer starts with the formation of small cavities known as crazes. The size of these crazes were determined to be of the order of a few nanometers for polypropylene by several small angle X-ray scattering studies and these results are also supported by molecular dynamics simulation of metallic glasses and glassy polymers [29, 30, 31, 32]. With further increase in strain, the polymer chains start to align and straighten themselves

which can be seen as a small plateau in the stress-strain curve where the stress is almost constant with increasing strain. On further increasing strain, the cavities/crazes are extended and the fibrils become more and more disentangled just before the yield point of the polymer [28, 31, 32]. The yield point of the polymer is shown as a black dashed line in Figure 2.3(a) after this point the polymer breaks and is unable to withstand the higher strain.

Figure 2.3(b) shows the plastic deformation region of HDPE film. In HDPE instead of having a well-defined plastic deformation plateau, there is a continuous decrease in the stress with an increase in strain also there is no definite yielding of the film which can also be seen from Figure 2.1(b). Since HDPE possesses a semicrystalline nature, there is a stacking of crystalline and amorphous regions. The crystalline domain possesses higher bond strength as compared to the amorphous domain. When this polymer undergoes a strain higher than its elastic limit, the plastic deformation starts by extension of the amorphous regions of the polymer which appears in the form of a small plateau in the strain-strain curve of HDPE which is shown in the initial region of Figure 2.3(b). On further increasing the strain, the chain molecules present in the crystalline region start to rotate in the direction of deformation and the crystalline part starts separating into different blocks which are also known as crystallographic slip popularly observed in wide-angle X-ray scattering of HDPE [33, 34]. The crystallographic slip often results in a decrease of the stress on increasing strain which is observed in HDPE films.

The plastic deformation region of LLDPE film is shown in Figure 2.3(c). Although LLDPE is a semi-crystalline polymer, the branched structure of LLDPE enables it to contain a higher number of amorphous domains than HDPE due to which the stress-strain curves for LLDPE show a behavior fluctuating between semi-crystalline and amorphous polymers. Here, the chain molecules are free to slide along each other due to the increase in specific volume and mobility of the molecules [28, 35]. Their behavior is similar to viscous liquids and as a result, the strength of the polymer is lower. But the polymer chain undergoes stretching and alignment of the amorphous domains in the direction of deformation. On further increase in strain, cavity formation is also observed similar to amorphous polymers which can be observed in the form of a small dip in the plateau region in figure 2.1(c). On further increasing strain, the cavities/crazes are extended and the fibrils become more and more

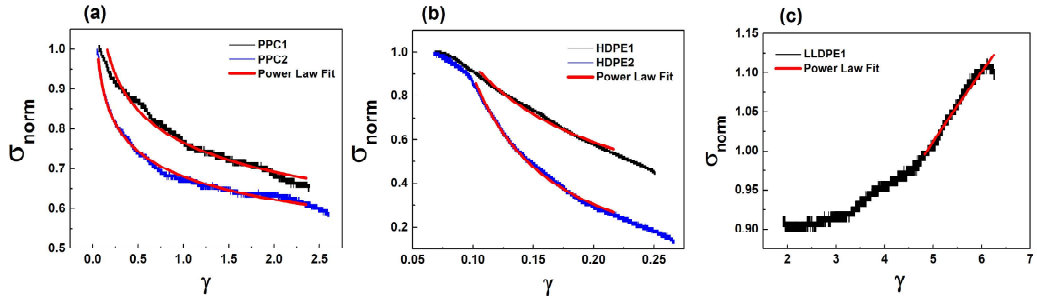

FIGURE 2.4: Plastic deformation region of stress-strain curves of (a) PPC, (b) HDPE, and (c) LLDPE for two different samples. The red curve shows the power law: $\sigma = K.\gamma^n$, with n = -0.14531 $\pm$ 0.000009 for PPC1 and n = -0.1283 $\pm$ 0.00004 for PPC2; n = -0.6838 $\pm$ 0.0004 for HDPE1 and n = -1.54 $\pm$ 0.00001 for HDPE2; n = 0.4649 $\pm$ 0.0003 for LLDPE1.

disentangled. The disentanglement becomes more intense with increasing strain and strain hardening is observed which is shown in Figure 2.3(c). It can also be seen from Figure 2.1(c) that the three different sets of LLDPE show different plastic behavior, this is because of the variable crystalline and amorphous content in the polymer film due to which LLDPE shows characteristics similar to semi-crystalline polymers as well as completely amorphous polymers.

Another interesting feature of the plastic response of the polymers is the power law dependence of the stress-strain curve in the plastic deformation region which is shown in Figure 2.4. In PPC and HDPE strain softening is observed (Figure 2.4(a) and (b)) but in LLDPE strain hardening is observed with increasing strain (Figure 2.4(c)). The difference in the plastic deformation of the polymers can also be due to the proximity of the polymers to glass transition temperature (T_g) [23]. At temperatures slightly near T_g like in PPC where the T_g is nearly 35 °C [36], the mean distance between the chain molecules is larger which enables them to partially overcome the binding forces and the molecules have limited mobility. The heat generated during deformation causes a local increase in temperature which results in local softening of the material which can be seen in Figure 2.4(a). When the temperature was far above the glass transition temperature like in the case of HDPE (T_g = -110°C, [37]) and LLDPE (T_g = -137 °C, [38]), the chain molecules can easily slide past each other which increases the mobility of the molecules.

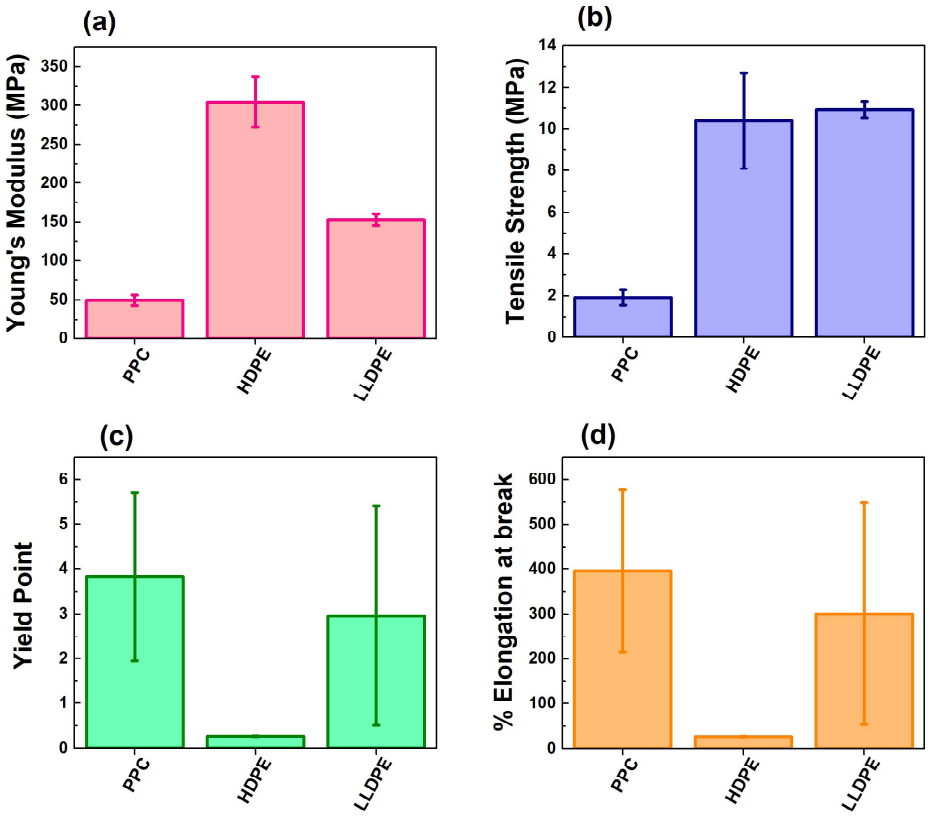

FIGURE 2.5: Mechanical properties (a) Young's modulus, (b) Tensile strength, (c) Yield point and (d) % Elongation at break of polymer films. The mechanical properties were calculated as a mean of the quantities obtained for all the samples and the errorbars represent the standard deviation.

2.4.3 Comparison of mechanical properties

TABLE 2.1: Mechanical properties (Young's modulus (YM), tensile strength (TS) and percentage elongation at break (PE)) for non-biobased non-biodegradable polymer (NB-NB), non-biobased biodegradable polymer (NB-BP), biobased nonbiodegradable polymer (BB-NB) and biobased biodegradable polymer (BB-BP), from previously published sources.

Non-Biobased Nonbiodegradable Polymers (NB-NB)					
	Material	YM (Mpa)	TS (Mpa)	Elongation (%)	Ref
1	PP	1747	35.6	28.17	[13]
2	PE	116.7	8.1	181.52	
3	PP (flax fiber)	3630	38.2	3.58	
4	PE	1639	15.3	3.72	
5	PP (hemp fiber)	2862	41.9	5.98	
6	PE	2094	21.2	3.03	
7	HDPE	790	18		[37]
8	HDPE	610	27		[39]
9	HDPE	733	28.8		[40]
10	HDPE	667	33		[41]
11	LLDPE	51	3.7		[42]
12	LLDPE	70	7.2		[43]
13	LLDPE	500	10	682.83	[44]
14	LLDPE	65.3	11.4	438.4	[45]
15	LLDPE	180	21.5	425	[46]
16	LLDPE	22	18.2	600	[47]

Non-Biobased Biodegradable Polymers (NB-BP)					
	Material	YM (Mpa)	TS (Mpa)	Elongation (%)	Ref
1	cellulose diacetate	2044	33.5	18.17	[13]
2	PHB (polyhydroxy butyrate)	1331	22.7	19.67	
3	PLA	3710	67.3	6.62	
4	cellulose diacetate (flax fiber)	4230	43.1	5.37	
5	PHB (polyhydroxy butyrate)	3621	22.9	4.63	
6	PLA	6197	64.4	6.21	
7	cellulose diacetate (hemp fiber)	4452	45.4	5.29	
8	PHB (polyhydroxy butyrate)	2421	21.4	4.2	
9	PLA	6750	71	5.81	[11]
10	PBS poly(butylenes succinate)	600		11.2	[48]
11	PLA	2600		1.9	
12	PHBV poly (3-hydroxybutyrate-co-3-hydroxyvalerate)	2500		3.8	
13	PLA/PBAT poly (butylene adipate-co-butylene terephthalate)	2164	48.1		[12]
14	PLA/PBAT/HRDP halloysite nanotubes resorcinol diphenyl phosphate (RDP)	2521	51.6		
15	HCS Hydroxypropyl cassava starch		1.8	37.5	[49]

16	HCS + waxy maize starch nanoparticles/κ-carrageenan		5.8	12	
17	PLA	2500	53		[50]
18	PLA + chitin	2800	85		
19	PLA + chitin + starch	2650	70		
20	PLLA (poly-L-lactic acid)	1894	68.1	5.07	[51]
21	PLLA+lignin	1888	46.8	3.25	[51]
22	PCL (polycaprolactone)	5000	20	1300	[52]
23	PGA (polyglyconic acid)	7GPa	115	3	[53]
24	PHB (polyhydroxy butyrate)	1.7-3.5 Gpa	40	6	
25	Poly (butylene succinate) (PBS)	3300	32.1	321	
26	PLA	1.2-2,7 GPA	28-50	9	
27	Poly(trimethylene carbonate) (PTMC)	50-60	1.8-2.4	610-670	
28	Poly (ϵ-caprolactone) (PCL)	4000	16	120-800	
29	PHBV Poly (3-hydroxybutyrate-co-3-hydroxyvalerate)	7000-2900	30-38	20	
30	PBAT Poly (butylene adipate-co-terephthalate)	400-800	11 - 20 Mpa	500-800	
31	PBSA Poly [(butylene succinate) -co- (butylene adiapate)]	1600	15.6	408	
32	PLGA Poly (L-lactide-co-glycolide)	2-4GPa	40-90	10	
33	PLCL Poly (lactide-co-caprolactone)	1340	17.2-26.6	314-486	
34	PGC Poly (glycolide-co-caprolactone)	4000-1700	0.6	250	
35	PLGC Poly (lactide-co-glycolide-co-caprolactone)	200	31.5	500	
36	PBS poly(butylenes succinate)	268	24.8	175.2	[54]
37	PEA (poly(ethylene adipate))	312.8	13.2	362.1	
38	polyurethane + castor oil	0.47	2.52	406	[55]
39	polyurethane + castor oil + glycerol	1.08	4.8	532	
40	polyurethane + glycerol	1.55	5.99	545	
41	PSU polysulfone	2.48	70.3		[56]
42	PES: polyethersulfone	2.6	83		
43	PPSU: polyphenylsulfone	2.3	70		
44	PEEK: polyetheretherketone	4	98		
45	PLA/starch	3517	33	1.2	[57]
46	PLA/starch	3420	32	1.5	
47	PLA/starch	3690	41	1.1	
48	PLA/starch	3543	46	3.3	
49	PLA/starch	3864	42	2.3	
50	PLA/starch	3969	38	1.3	
51	PLA/starch	4069	35	1.3	
52	PPC	101	4.8		[58]
53	PPC	417	10.5	325	[59]
54	PPC	392	31	3.8	[2]

Biobased Biodegradable Polymers (BB-BP)

	Material	YM (Mpa)	TS (Mpa)	Elongation (%)	Ref
1	corn starch bioplastic	58	3.3	100	[9]
2	corn starch + polyvinyl alcohol	15	10	300	
3	polyvinly alcohol (PVA)	3	20	800	
4	Guar gum		40.73		[60]

5	Guar gum + chitosan		37.33		
6	Guar gum chitosan composite		39		
7	Grass pea flour films	26.2	0.7	32.2	[10]
8	Grass pea flour films + microbial transglutaminase	17.1	1.04	59.1	
9	wheat protein isolate	811		13.9	
10	wheat protein isolate + silk fiber	1605		3.4	
11	Corn starch	52	2.5		[61]
12	Corn starch + clay	200	5		
13	Corn starch + Ag + clay	400	6.2		
14	CS + Cu + clay	270	5.5		
15	Potato starch gelatinized	923	33.45		[62]
16	PS precured	1359.8	35.5		[62]
17	PS cured	2701	23.17		[62]
18	Flex	50-70 Gpa	345-1500	2.7-3.2	[63]
19	Hemp	70	690	1.6	
20	Jute	13-26.5	393-800	1.16-1.5	
21	Remi	61.4-128	400-938	1.2-3.8	
22	Sisal	9.4-22	468-700	3.0-7.0	
23	Cotton	5.5-12.6	287-800	7.0-8.0	
24	Silk	10	600	20	
25	Spider silk	7.2-9.2	800-1000	30-60	
26	Basalt	35	3050		
27	Asbestos	0.4-2	550-750		
28	E-glass	29	3400	2.5	

Biobased Nonbiodegradable polymer (BB-NB)					
	Material	YM (Mpa)	TS (Mpa)	Elongation (%)	Ref
1	PE	8500	35	7	[64]
2	PTT	23000	65	8	[64]
3	PP	121	5	2.5	[7]
4	Recycled PE	117	5	2.7	
5		119	5.8	3.2	
6		123	6	3.3	
7		114	5.9	2.9	
8		87	3.3	2	
9	PP + starch	73	5	3.4	
10		82	5.5	3.7	
11		56	5.2	4	
12		80	5.5	3.7	
13		95	5.2	3.7	
14	PA	2880	75.5	100	
15	PA/cnt	2850	74.3	7	[65]
16		2860	75.6	7	
17		2870	74.3	5	
18		2930	75.1	7	
19		3010	74.5	5	
20		3010	76.3	6	
21	Bio-PET	777	50	378.4	[3]
22	Bio-PET + cotton fiber	843	48.1	8.1	
23		898	42	6.5	
24		907	39	6.2	

25	907	36	5.7
26	950	30	4.2
27	1124	24	2.8

The mechanical properties of polymer films are extracted from the stress-strain curves and are represented in the form of a bar graph in Figure 2.5. The Young's modulus is highest for HDPE (Figure 2.5(a)) which is approximately 200 MPa higher than LLDPE. On the other hand, the tensile strength (Figure 2.5(b)) is almost the same for both HDPE and LLDPE. A possible explanation for this is the presence of higher crystallinity in HDPE as compared to LLDPE. PPC on the other hand shows lower Young's modulus and tensile strength as compared to HDPE and LLDPE but being a biodegradable polymer and completely amorphous, PPC showed substantially strong tensile properties which are comparable to the commercial HDPE and LLDPE. Although PPC had weaker elastic properties in comparison to HDPE and LLDPE, the plastic properties like yield point and elongation at break are larger which makes it a suitable candidate for adhesive materials. The yield point (Figure 2.5(c)) and % elongation at break (Figure 2.5(d)) are highest in PPC indicating that PPC films can withstand a larger amount of strain as compared to HDPE and LLDPE.

Young's modulus, tensile strength, and elongation at break of PPC are also compared with other non-biodegradable and biodegradable polymers which have previously been synthesized and studied for bioplastic applications which are discussed in Table 2.1. A two-component principal component analysis of the tensile properties of several non-biobased non-biodegradable (NB-NB), non-biobased biodegradable (NB-BP), biobased non-biodegradable (BB-NB) and bio-based biodegradable (BB-BB) polymers was performed which is shown in Figure 2.6. The tensile properties from the present study are highlighted in green (for polyethylene) and purple (for PPC). From Figure 2.6 it can be observed that the mechanical properties of PPC match with the currently available literature on polymers from various origins. Therefore, it is safe to state that PPC can be used as an alternative to non-biodegradable polymers.

The comparison of mechanical properties of the polymers shows that each polymer has a different mechanical response (both elastic and plastic) which was dependent on two important factors - the amount of crystalline/amorphous

content in the polymer and the vicinity of the glass transition temperature. Also, the response to mechanical perturbation of polymers is accompanied by several microscopic mechanisms like crack formation, crazing, crystallographic slip, cavity formation, etc. which are responsible for the difference in the mechanical properties. Reorientation of the crystalline and amorphous domains via stretching or rotation is the first step when any polymer undergoes mechanical perturbation which has also been observed in HDPE with the help of Wide-angle X-ray scattering experiments [35]. Deformation-induced molecular mobility has also been observed in PMMA glass which was found to be highly heterogeneous consisting of domains that were moving faster than others under strain [66, 67]. Deformation in polymer glasses has also been found to induce nanoscopic motions experimentally via inelastic and elastic neutron scattering [68]. Also, the inhomogeneities in the micro-structures can affect the global plasticity and failure of the films [69]. The mechanical properties of polymers are dependent on the inter-molecular bonds between the chains which undergo reorientation under deformation, thereby influencing molecular mobility [67] and the micro-structures formed under perturbation [69]. It is therefore important to study the microscopic as well as molecular-level mechanisms taking place in polymers under perturbation to understand the overall macroscopic behavior of the polymers. This was analyzed with the help of Raman scattering in aging polymers after the thermal quench.

2.5 Raman spectroscopy

2.5.1 Theoretical background

Raman spectroscopy is a vibrational spectroscopy that depends on the interaction of electromagnetic radiation with the vibrating molecule. Raman spectroscopy or Raman scattering demonstrates the interaction of electromagnetic radiation with matter, during this interaction, some amount of energy is transferred between the photons and molecular vibrations, and the photons are scattered with a frequency different from the frequency of incident electromagnetic radiation.

When a molecule is positioned in an electric field, an electrical dipole moment is induced in the system which is given by :

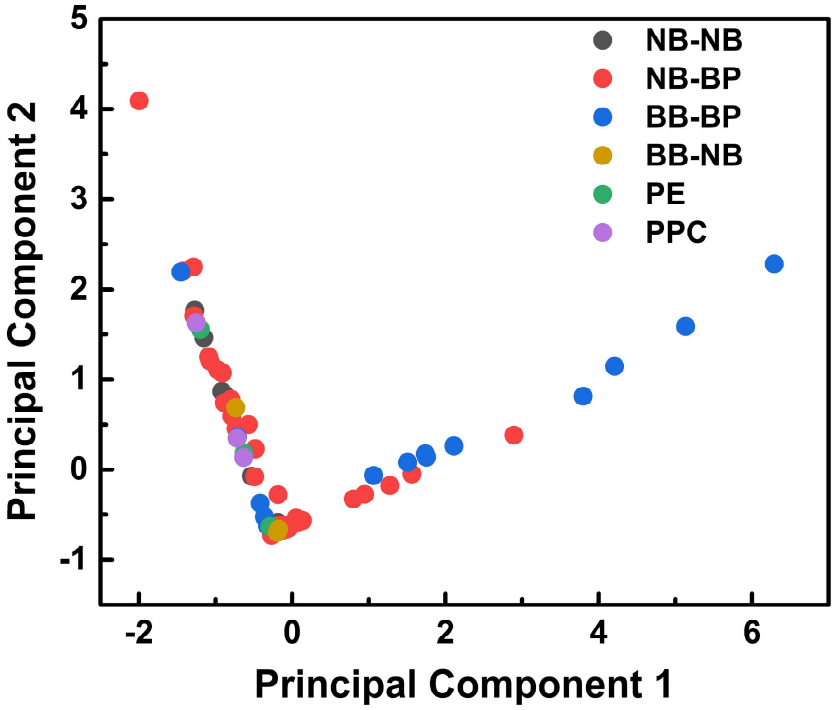

FIGURE 2.6: Two-component principal component analysis for the tensile properties (Young's modulus, tensile strength, and % elongation at break) for non-biobased nonbiodegradable (NB-NB), non-biobased biodegradable (NB-BP), biobased nonbiodegradable (BB-NB) and biobased biodegradable (BB-BP) polymers. The experimental observation for polyethylene (PE) and polypropylene carbonate (PPC) and highlighted in green and purple respectively.

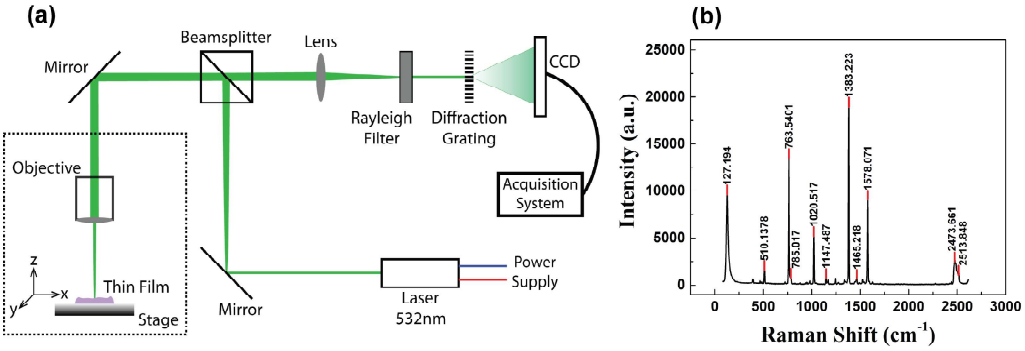

FIGURE 2.7: (a) Schematic of Raman spectrometer (b) Calibration curve using Naphthalene crystals.

$$p = \alpha.E \tag{2.3}$$

In the above equation, α is the polarizability. While studying the Raman effect, the electric field of the electromagnetic radiation and the polarizability α tensor which depends on the shape and dimensions of the chemical bonds, interact and change during vibrations. Therefore, the polarizability depends on the molecular vibrations and a change in molecular vibrations changes the polarizability which is the condition for observing the Raman spectrum. The polarizability tensor (α) is thus dependent on the normal coordinate Q of the molecule which corresponds to the normal mode of vibration. If the incident radiation has a vibrational frequency (ν_0) and the molecule has a vibrational frequency (ν_ν), then the induced dipole moment can be split into three components:

$$p = p(\nu_0) + p(\nu_0 + \nu_\nu) + p(\nu_0 - \nu_\nu) \tag{2.4}$$

The first term in the above equation indicates elastic scattering and it is due to the elastic scattering from the molecules with no change in frequency (hence the same energy). This is known as Rayleigh scattering. The second and third terms correspond to the inelastic scattering of the light involving a change in frequency, which is attributed to Raman scattering. The second term, when the scattered frequency is higher than the frequency of incident radiation, it is called Anti-Stoke's Raman scattering and the third term when the scattered frequency is lower than the frequency of incident radiation is called Stoke's Raman scattering. The most intense and commonly observed is Stoke's Raman scattering. The modes of vibration present in a molecule can be Raman active or inactive depending on a set of selection rules which determine whether the mode is Raman active and how observed spectral features can be assigned to normal modes. Any mode can be Raman active if it experiences a change in polarisability during interaction with electromagnetic radiation.

Usually, in a Raman spectrum, the intensity is plotted as a function of the Raman wavenumber ω, expressed in cm^{-1}, which is related to the difference in frequency between the scattered light and the incident electromagnetic radiation. According to the harmonic oscillator approximation, the molecular bonds can be considered as a harmonic oscillator: a diatomic molecule is represented as two

balls connected with a spring which follows Hooke's law. As a consequence, the vibrational frequency of the Raman band can then be expressed in terms of the force constant (k) and reduced mass (μ) of a spring mass system which can be expressed as:

$$\nu_\nu = \frac{1}{2\pi}\sqrt{\frac{k}{\mu}} \tag{2.5}$$

Therefore, two factors that determine the Raman band position are the force constant of the bond and the type of vibration (k), and the reduced mass (μ). Once these two properties are known, the Raman band position can be calculated and vice versa. Since the force constant is strongly dependent on the inter and intramolecular interactions, the type of bonding can cause a band shift in the Raman spectrum. Also, the electron donors or electron acceptors influence the electron density of the bond, and thus also its force constant, which is observed as a shifting Raman band.

The overall intensity of the Raman band is divided into two groups:

$$I = \alpha.\beta \tag{2.6}$$

where β contains the parameters related to an instrument like the intensity of source radiation and detector efficiency and α contains the parameters related to the sample like the contribution of the molecules. The total Raman intensity equals the sum of the contributions of all molecules in the analyzed volume V. When considering a group of randomly oriented molecules, the intensity has to be averaged over all possible orientations (α_{xx}, α_{yy} and α_{zz}) of the system, in relation to the considered electrical field. Therefore, the intensity of the Raman spectrum is dependent on the number of molecules contributing to the vibrational state and there is a linear relationship between the measured intensity and the number of molecules in the sampled volume. The Raman signal can further be enhanced by following time-dependent effects like resonance enhanced Raman effect.

Along with Raman band position and intensity, another important factor that provides insight into the vibrational properties of the material is the Raman bandwidth. An important source of band broadening in the Raman band is the local molecular neighborhood, which can be amorphous or crystalline. The

Raman bands of amorphous materials are broader than the crystalline materials. Band broadening can also be observed due to the presence of isotopes, the difference in atomic mass is reflected at different band positions which are closer than the spectral resolution, leading to band broadening.

2.5.2 Raman instrumentation

The Raman spectrometer consists of four main parts: a light source, a sample stage, a dispersion system, and a detector. The components for each part have to be selected according to the tasks and options that are chosen. There are two important types of Raman spectrometer: a dispersive spectrometer which uses grating for the separation of light and its components and a Fourier-transform (FT) Raman spectrometer which uses a Michelson interferometer. For the present study, a highly sophisticated and well-equipped confocal Raman spectrometer was used which was operating in backscattered geometry. The spectrometer was supplied by AIRIX corporation and the model was STR300. A schematic of the Raman spectrometer used is shown in Figure 2.7(a). The light source for the spectrometer was a DPSS laser (Quantum gem) with a 532 nm excitation wavelength. Appropriate neural density filters were applied to maintain the laser power to 50 mW. The laser beam which was used for excitation was passed through a 20X-0.40NA ELWD Nikon objective to maintain a sharp focus of the beam on the films placed on the sample stage. The light which was scattered through the sample was also collected through the same objective. The scattered light then passes through the dispersion system consisting of a beam splitter, a set of lenses and filters, and finally through the diffraction grating to separate different frequencies from the scattered light. To detect the scattered light Andor iDus Peltier cooled CCD detector (cooled to 203 K) was used which was connected to an acquisition system software in a computer that plots the Raman spectrum.

For thermal quench experiments, the sample was placed inside a Linkam THMS600 temperature controller stage which was operated using software for the application of the desired temperature. Inside the temperature controller, the Nitrogen atmosphere was maintained. Liquid nitrogen was used to maintain temperatures below room temperature and a separate heating unit was used to maintain temperatures above room temperature. The Raman spectra were

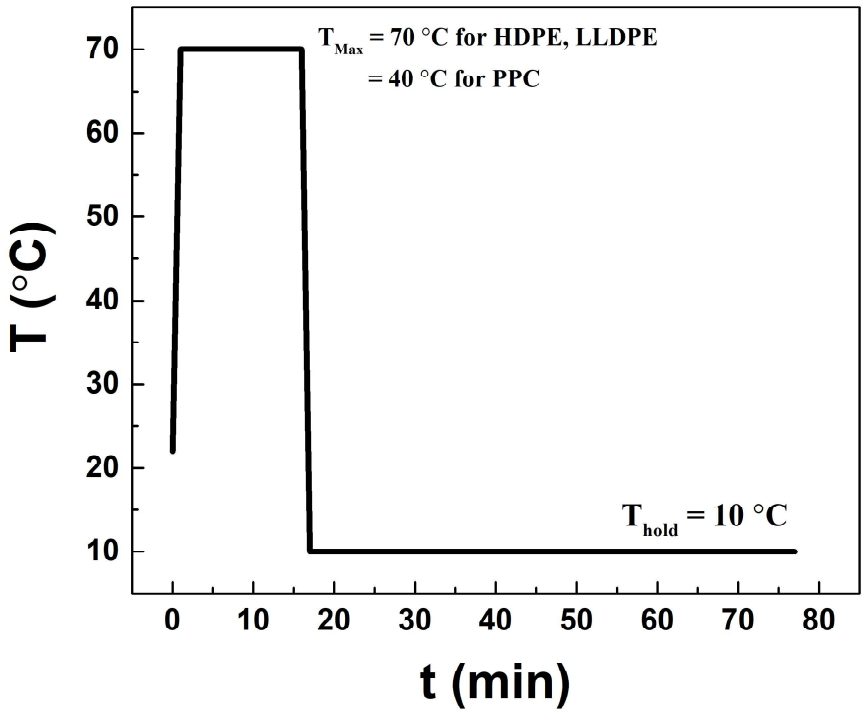

FIGURE 2.8: The thermal quench applied to the polymer films. T_{Max} is the maximum temperature to which the films are heated, and T_{hold} is the temperature at which the films are maintained after quenching.

collected in a spectral range of 500 cm^{-1} - 3100 cm^{-1} with two acquisitions of 30 secs. each which were averaged to obtain the final spectrum.

2.5.3 Methodology for thermal quench

To study the effect of the thermal perturbation on the polymer films, the films were subjected to a thermal quench which is shown in Figure 2.8. Raman spectrum was collected at room temperature at the beginning of the thermal cycle. Then the sample was heated up to T_{Max} at the rate of 20 °C/min and was maintained at the same temperature for 15 minutes. For HDPE and LLDPE films T_{Max} = 70 °C and for PPC films T_{Max} = 40 °C because PPC undergoes thermal degradation beyond 50 °C. Heating the samples upto T_{Max} was done to erase

any thermal history present within the polymer film. Raman spectrum was also collected at T_{Max}. After 15 minutes the sample was quenched with the rate of 60 °C/min up to T_{hold} = 10 °C and was maintained at the same temperature for 60 minutes. Raman spectra were collected as a function of waiting time after quench (t_w) at an interval of 5 minutes from t_w = 0 minutes to 60 minutes.

2.5.4 Data collection and analysis

The instrument was first calibrated using naphthalene crystals and the calibration curve is shown in Figure 2.7(b). The data was collected using a built-in software - STP data collection software supported by the spectrometer and the data was analyzed using Origin^{TM} software. The Raman spectrum then obtained for polymer films was corrected for background by detrending using a polynomial function and the minimum baseline obtained was subtracted from the original spectrum. For the corrected data, the Raman peaks were then extracted individually and were fitted using a non-linear least square fitting operation and the best fit was determined for all the peaks. The Lorentzian function (Equation 2.7) was obtained as the best fit for all the peaks in all three polymer films with a minimum standard deviation χ^2 and coefficient of determination $R^2 > 0.9$.

$$I = I_0 + \frac{2Aw}{4\pi(x - x_c)^2 - w^2} \tag{2.7}$$

In the above equation, I is the Raman intensity, I_o is constant, x represents the Raman shift (in cm^{-1}), x_c is the Raman peak center (in cm^{-1}), w is the full width at half maximum (FWHM in cm^{-1}), and A is the area under the peak.

2.6 Effect of thermal perturbation

When a polymer is subjected to thermal perturbation, the polymer starts aging, which is sensitive to waiting time after the quench (t_w). Experiments and simulations on colloidal glass formers have seen that aging manifests molecular segmental dynamics in the case of polymers [20, 21, 24, 70]. To study the effect of thermal perturbation, the polymer films were subjected to a thermal quench passing through the glass transition temperature as shown in Figure 2.8. The

TABLE 2.2: Raman modes corresponding to peaks observed in the Raman spectrum of HDPE, LLDPE, and PPC films. The peak center is determined from the Lorentzian fitting of the Raman peaks and the corresponding vibrational mode is determined from the fingerprints available in literature [4, 71, 72]

PPC		HDPE		LLDPE	
Peak center (cm^{-1})	Assignment	Peak center (cm^{-1})	Assignment	Peak center (cm^{-1})	Assignment
863	C-C doublet stretching	1060	C-C anti-symmetric stretching	1062	C-C anti-symmetric stretching
883	C-C doublet stretching	1088	C-C symmetric stretching (gauche mode)	1085	C-C symmetric stretching (gauche mode)
917	C-C stretching in branch	1127	C-C symmetric stretching (trans mode)	1128	C-C symmetric stretching (trans mode)
963	C-C stretching in C-CH_3	1292	CH_2 in phase twisting / C-C twisting	1293	CH_2 in phase twisting / C-C twisting
1072	C-C anti-symmetric stretching	1412	CH_2 wagging	1413	CH_2 wagging
1114	C-O-C symmetric stretching	1435	CH_2 bending	1437	CH_2 bending
1167	C-O stretching	1459	CH_2 scissoring	1457	CH_2 scissoring
1352	C-H deformation	2842	C-H symmetric stretching	2843	C-H symmetric stretching
1457	CH_2 scissoring	2875	C-H symmetric stretching	2876	C-H symmetric stretching
1750	C=O stretching	2883	C-H symmetric stretching	2892	C-H symmetric stretching
2885	C-H symmetric stretching				
2907	C-H symmetric stretching				
2944	C-H asymmetric stretching				
2966	C-H asymmetric stretching				
2998	C-H asymmetric stretching				

Raman spectrum of polymer films was observed at different points during the thermal cycle (explained in section 2.5.3) to study the effect of the thermal perturbation on the molecular vibrations of PPC, HDPE, and LLDPE films.

2.6.1 PPC

Figure 2.9(a) shows the Raman spectrum at room temperature for PPC film. The vibrational modes present at room temperature are extracted from the Raman spectrum and fitted with a Lorentzian function. The Raman spectrum of PPC consists of various Raman bands which are deconvoluted into consecutive peaks. The first Raman band appearing between 750 cm^{-1} to 1000 cm^{-1} is deconvoluted into four peaks represented as peaks 1, 2, 3, and 4 in Figure 2.9(b). Peak 1 and peak 2 centered at 863 cm^{-1} and 883 cm^{-1} corresponds to the C-C doublet stretching vibrational mode; peak 3 centered at 917 cm^{-1} represents C-C stretching mode in branch and peak 4 centered at 962 cm^{-1} corresponds to C-C stretching mode in C-CH_3 mode of the polymer chain. Figure 2.9(c) represents the deconvolution of peaks 5, 6, and 7 where peak 5 has a peak center at 1072 cm^{-1} corresponding to C-C antisymmetric stretching, peak 6 has a peak center at 1114 cm^{-1} corresponding to C-O-C stretching mode and peak 7 centered at 1167 cm^{-1} corresponding to C-O stretching vibrations. Two closely appearing peaks with peak centers at 1352 cm^{-1} and 1457 cm^{-1} corresponding to C-H deformation and CH_2 scissoring modes are shown in Figure 2.9(d). The peak corresponding to C=O stretching vibrations present in the side branch of the

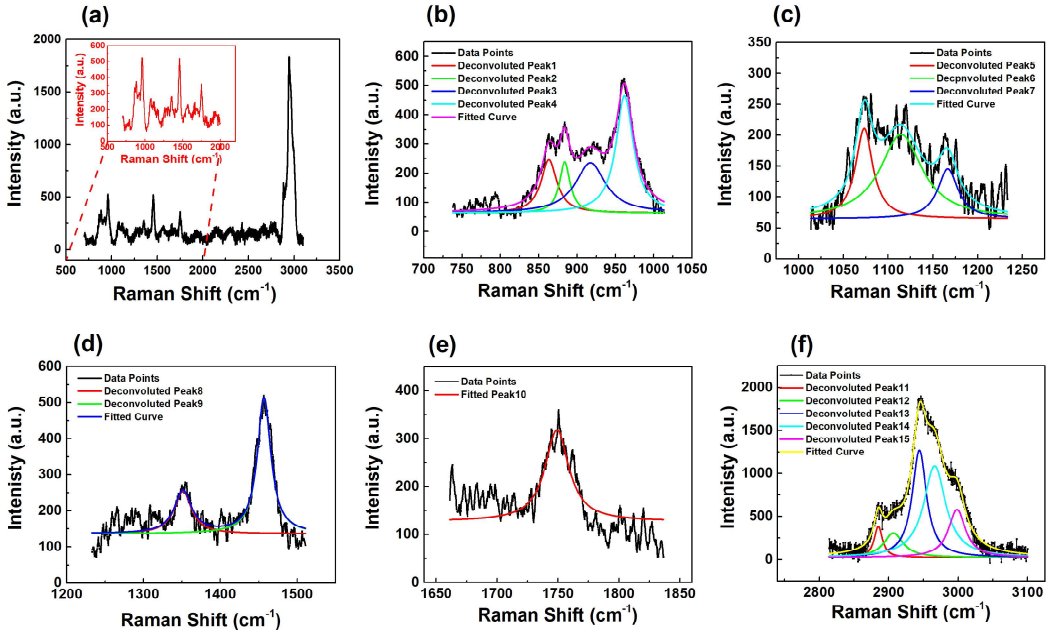

FIGURE 2.9: (a) Raman spectrum at room temperature (25 °C) of PPC film representing the vibrational modes presented as peaks in the Raman spectrum. The inset in (a) represents Raman bands which can be deconvoluted into various Raman peaks. (b) represents deconvolution of the band between 750 cm^{-1} to 1000 cm^{-1} into peak 1, 2, 3 and 4 (c) represents deconvolution of the band between 1000 cm^{-1} to 1200 cm^{-1} into Peak 5, 6 and 7 (d) represents two closely appearing peaks at 1350 cm^{-1} (peak 8) and at 1460 cm^{-1} (peak 9) (e) represents peak 10 at cm^{-1} and (f) represents deconvolution of Raman band between 2800 cm^{-1} to 3100 cm^{-1} into peak 11, 12, 13, 14 and 15. All the peaks are found to fit well with the Lorentzian function (Equation 2.7).

polymer is shown in Figure 2.9(e) with peak center at 1750 cm^{-1}. The most intense peak in the Raman spectrum of PPC is between 2800 cm^{-1} to 3100 cm^{-1} representing the C-H stretching vibrational mode which is present in both the main chain and side branch of the polymer. Figure 2.9(f) shows the deconvolution of the Raman band for C-H stretching vibrations into peaks 11, 12, 13, 14, and 15. Peak 11 and peak 12 centered at 2885 cm^{-1} and 2907 cm^{-1} respectively correspond to C-H symmetric stretching modes and peaks 13, 14, and 15 correspond to C-H asymmetric stretching modes. All the peaks are best fitted with a Lorentzian function and the peak parameters - peak center, full width at half maximum (FWHM), integrated peak intensity or area under the peak (I_{INT}), and peak height (I_{Max}) are extracted from the fitting data.

The effect of temperature quench on PPC film is studied by critically analyzing the time evolution after a quench of the peak fit parameters for different modes present in the Raman spectrum of PPC. Peak 4, peak 10, and peak 13 corresponding to the C-C stretching mode present in the main chain of the polymer, the C=O stretching mode present in the side branch of the polymer, and the C-H stretching mode present in both the main and side branch of the polymer respectively are chosen to gain information about the overall behavior of the polymer as a function of waiting time after quench (t_w). Figure 2.10(a) represent the Lorentzian fitting of peak 4 corresponding to C-C stretching vibrational mode and the temporal evolution of the peak parameters is shown in Figure 2.10(b)-(e). A prominent change in the form of fluctuations is observed in the peak fit parameters as a function of t_w. The peak center shows random fluctuations, within the errorbars (Figure 2.10(b)) but the peak FWHM shows a decrease of ≈ 6 $cm^{-}1$ as a function of t_w. The I_{INT} and I_{Max} also show a decrease as a function of t_w. The decrease in I_{INT} and I_{Max} corresponds to a decrease in the number of contributing molecules for the C-C stretching mode as a function of t_w whereas the decrease in FWHM represents band narrowing which can be correlated with a decrease in molecular mobility in the polymer matrix [73].

For peak 10 corresponding to C=O stretching mode (Figure 2.11(a)), the peak fit parameters show random fluctuation with t_w. The peak center shows a variation of 2 cm^{-1} (Figure 2.11(b)) and the peak FWHM fluctuates (Figure 2.11(c)) between $\pm$ 3 cm^{-1}. These random fluctuations in FWHM are the signature of random mobility in the polymer matrix. The I_{INT} (Figure 2.11(d))and I_{Max} (Figure 2.11(e)) also fluctuates with t_w, although there is no

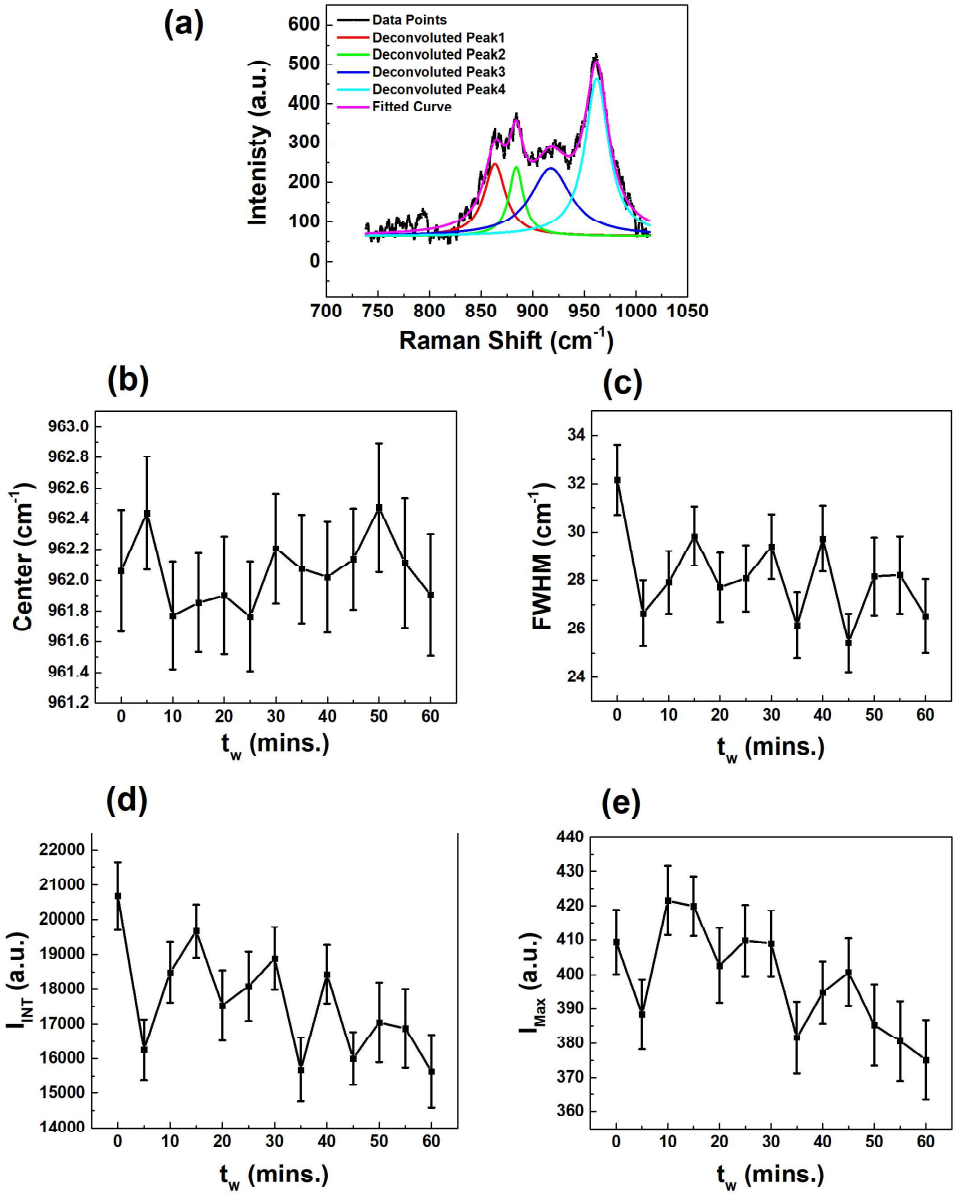

FIGURE 2.10: (a) The Raman band appearing between 750 cm^{-1} to 1000 cm^{-1} for PPC film is deconvoluted into four peaks, peaks 1, 2, 3, and 4 using the Lorentzian function. (b), (c), (d), and (e) show respectively the time evolution of the peak center, the full width at half maximum (FWHM) of the peak, the integrated peak intensity or the area under the peak (I_{INT}) and the maximum peak intensity (I_{Max}) for peak 4 corresponding to C-C stretching mode present in the main chain of the polymer.

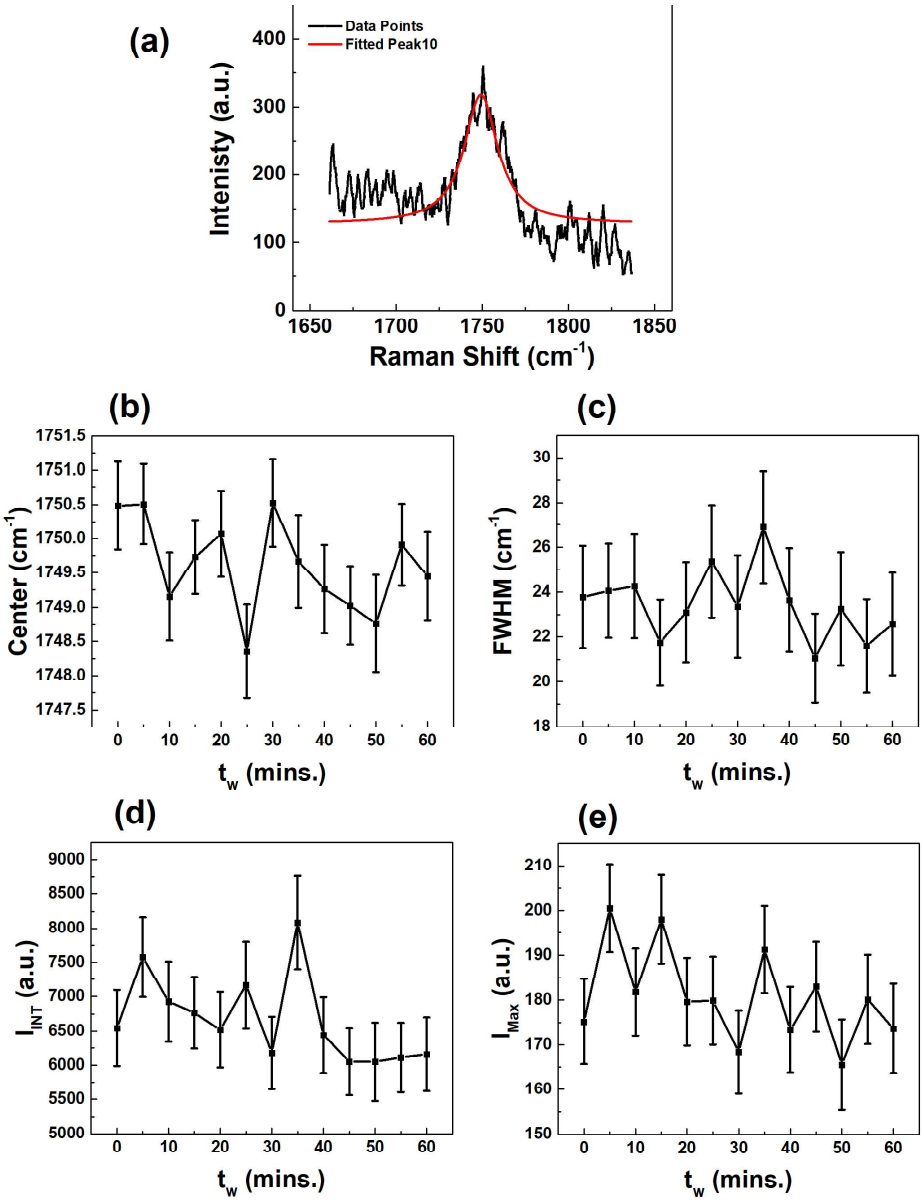

FIGURE 2.11: (a) The Raman peak appearing at 1750 cm^{-1} for PPC film corresponding to C=O stretching mode present in the side branch of the polymer fitted with a Lorentzian function. (b), (c), (d), and (e) show respectively the time evolution of the peak center, the full width at half maxima (FWHM) of the peak, the integrated peak intensity or the area under the peak (I_{INT}) and the maximum peak intensity (I_{Max}) for the peak.

significant change. The fluctuations indicate variations in the contributing bonds for the C=O stretching Raman mode. The peak parameters for peak 10 also remain mostly unaffected when studied as a function of t_w indicating that the modes present in the side branch of the polymer are less prone to the thermal perturbation as compared to the modes present in the main chain of the polymer-like peak 4.

The peak 13 representing C-H stretching modes, which are present in both the main chain and side branch of the polymer is shown in Figure 2.12(a). The peak center (Figure 2.12(b)) and FWHM (Figure 2.12(c)) for peak 13 show a similar character as peaks 4 and 10 with random fluctuations as a function of t_w with a variation of $\pm$ 1 cm^{-1} in peak center and a variation of $\pm$ 3 cm^{-1} in FWHM. The I_{INT} (Figure 2.12(d)) and I_{Max} (Figure 2.12(e)) on the other hand show a decreasing character with t_w similar to peak 4. The decrease in I_{INT} and I_{Max} is therefore, the signature of the decrease in the number of contributing molecules.

2.6.2 HDPE

The Raman spectrum for HDPE film at room temperature is divided into two regions: region 1 varying from 850 cm^{-1} to 1900 cm^{-1} as shown in Figure 2.13(a) and region 2 varying between 2300 cm^{-1} to 3100 cm^{-1} as shown in Figure 2.13(b). In region 1 the C-C stretching vibrational modes are present in the form of three closely appearing peaks which are deconvoluted into peaks 1, 2, and 3 at 1060 cm^{-1}, 1088 cm^{-1} and 1127 cm^{-1} respectively (Figure 2.13(c)). Peak 1 corresponds to C-C antisymmetric stretching mode, peak 2 corresponds to the gauge mode of C-C symmetric stretching, and peak 3 corresponds to the trans mode of C-C symmetric stretching present in the main chain of the polymer. A peak corresponding to CH_2 in phase twisting and C-C twisting is found at 1192 cm^{-1} (Figure 2.13(d)). The peaks corresponding to CH_2 wagging, CH_2 bending, and CH_2 scissoring present in the side chain of the polymer are deconvoluted from a Raman band into peaks 5, 6 and 7 at peak centers 1412 cm^{-1}, 1435 cm^{-1} and 1459 cm^{-1} respectively. In region 2 the Raman band corresponding to C-H stretching mode (Figure 2.13(e)) is deconvoluted into peaks 8, 9, and 10 with peak centers at 2842 cm^{-1}, 2875 cm^{-1} and 2883 cm^{-1} respectively corresponding

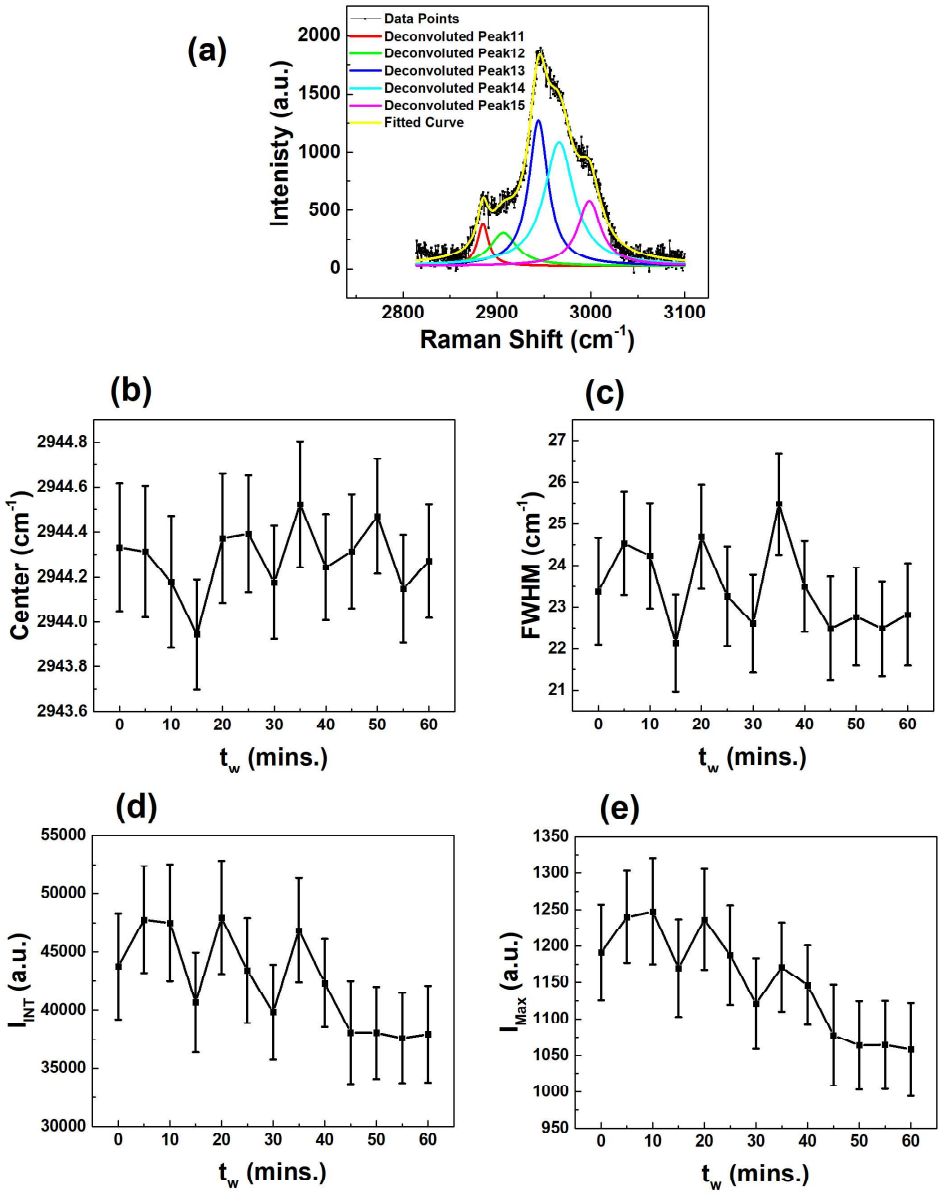

FIGURE 2.12: (a) The Raman band appearing between 2800 cm^{-1} to 3100 cm^{-1} for PPC film is deconvoluted into five peaks: peak 11, 12, 13, 14, and 15 using the Lorentzian function. (b), (c), (d), and (e) show respectively the time evolution of the peak center, the full width at half maxima (FWHM) of the peak, the integrated peak intensity or the area under the peak (I_{INT}) and the maximum peak intensity (I_{Max}) for peak 13 corresponding to C-H asymmetric stretching mode present in the main chain as well as a side branch of the polymer.

to C-H stretching vibrational modes present in the main chain and side chain of the polymer.

The effect of the thermal perturbation on HDPE film is determined from three main peaks: peak 3 corresponding to C-C symmetric stretching mode present in the main chain of the polymer, peak 5 corresponding to CH_2 wagging mode present in the side chain of the polymer, and peak 8 corresponding to C-H symmetric stretching mode present in both main chain and the side chain of the polymer. The C-C stretching mode (peak 3) of HDPE film is shown in Figure 2.14(a). The peak center for peak 3 in HDPE film (Figure 2.14(b)) shows random fluctuations with a variation of ± 0.4 cm^{-1} and peak FWHM (Figure 2.14(c)) shows a slight decrease of 1.5 cm^{-1} for 25 minutes and then increases by 1.5 cm^{-1}, this band narrowing followed by band broadening indicates the changing mobility at the molecular level. The I_{INT} (Figure 2.14(d)) and I_{Max} (Figure 2.14(e)) on the other hand show an increase with increasing t_w with a peak between 20-30 minutes and then starts decreasing with further increase in t_w. An increase in I_{INT} and I_{Max} corresponds to an increase in the number of contributing molecules that are excited and a decrease in I_{INT} and I_{Max} indicates a decrease in the number of contributing molecules.

For peak 5 (Figure 2.15(a)), the peak center shows a slight increase of 1 cm^{-1} with an increase in t_w as shown in Figure 2.15(b). The FWHM on the other hand shows random fluctuation with a slight increase of 1.5 cm^{-1} (Figure 2.15(c)) indicating random mobility fluctuations of the polymer matrix. The I_{INT} (Figure 2.15(d)) and I_{Max} (Figure 2.15(e)) on the other hand show a characteristic similar to peak 3 with an increasing character as a function of t_w having maxima between 20-30 minutes and then starts decreasing with further increase in t_w. An increase in I_{INT} and I_{Max} corresponds to an increase in the number of contributing molecules that are excited and a decrease in I_{INT} and I_{Max} indicates a decrease in the number of contributing molecules.

The peak 8 (Figure 2.16(a)) of region 2 corresponding to C-H stretching modes show random fluctuations in peak center (Figure 2.16(b)) and FWHM (Figure 2.16(c)) as a function of t_w after the quench. But the I_{INT} (Figure 2.16(d)) and I_{Max} (Figure 2.16(e)) shows prominent increase with increase in t_w. This characteristic indicates a strong increase in the number of contributing molecules for C-H stretching modes. The variation in the peak fit parameters of HDPE strongly suggests that even a small thermal perturbation can drive

fluctuations at the molecular level in an extremely rigid HDPE film. The overall comparison of peaks 3, 5, and 8 suggest that the modes attached to the main chain of the polymer are more affected by the thermal cycle in comparison to the modes present in the side chain of the polymer.

2.6.3 LLDPE

The Raman spectrum for LLDPE film at room temperature, similar to the Raman spectrum for HDPE film, is divided into two regions: region 1 varying from 850 cm^{-1} to 1900 cm^{-1} as shown in Figure 2.17(a) and region 2 varying between 2300 cm^{-1} to 3100 cm^{-1} as shown in Figure 2.17(b). In region 1 the C-C stretching vibrational modes are present in the form of three closely appearing peaks which are deconvoluted into peaks 1, 2, and 3 at 1062 cm^{-1}, 1085 cm^{-1} and 1128 cm^{-1} respectively (Figure 2.17(c)). Peak 1 corresponds to C-C antisymmetric stretching mode, peak 2 corresponds to the gauge mode of C-C symmetric stretching, and peak 3 corresponds to the trans mode of C-C symmetric stretching present in the main chain of the polymer. A peak corresponding to CH_2 in phase twisting and C-C twisting is found at 1193 cm^{-1} (Figure 2.17(d)). The peaks corresponding to CH_2 wagging, CH_2 bending, and CH_2 scissoring present in the side chain of the polymer are deconvoluted from a Raman band into peaks 5, 6 and 7 at peak centers 1413 cm^{-1}, 1437 cm^{-1} and 1457 cm^{-1} respectively. In region 2 the Raman band corresponding to C-H stretching mode (Figure 2.17(e)) is deconvoluted into peaks 8, 9, and 10 with peak centers at 2843 cm^{-1}, 2876 cm^{-1} and 2892 cm^{-1} respectively corresponding to C-H stretching vibrational modes present in the main chain and side chain of the polymer.

The Raman spectrum of LLDPE shows the same vibrational modes as are observed in HDPE but with a slight shift in wavenumbers because of the presence of long branches in LLDPE. Also, the peaks appearing in the Raman spectrum of LLDPE were broad whereas the Raman spectrum of HDPE film contains sharp Raman peaks. The broadening of peaks is due to the increase in amorphous character due to chain branching in LLDPE as compared to HDPE. Another characteristic of chain branching can be seen from the Raman peak intensities (I_{Max}) of the branched and linear polyethylene, on comparing the peak intensities of all the peaks present in the Raman spectrum of LLDPE and

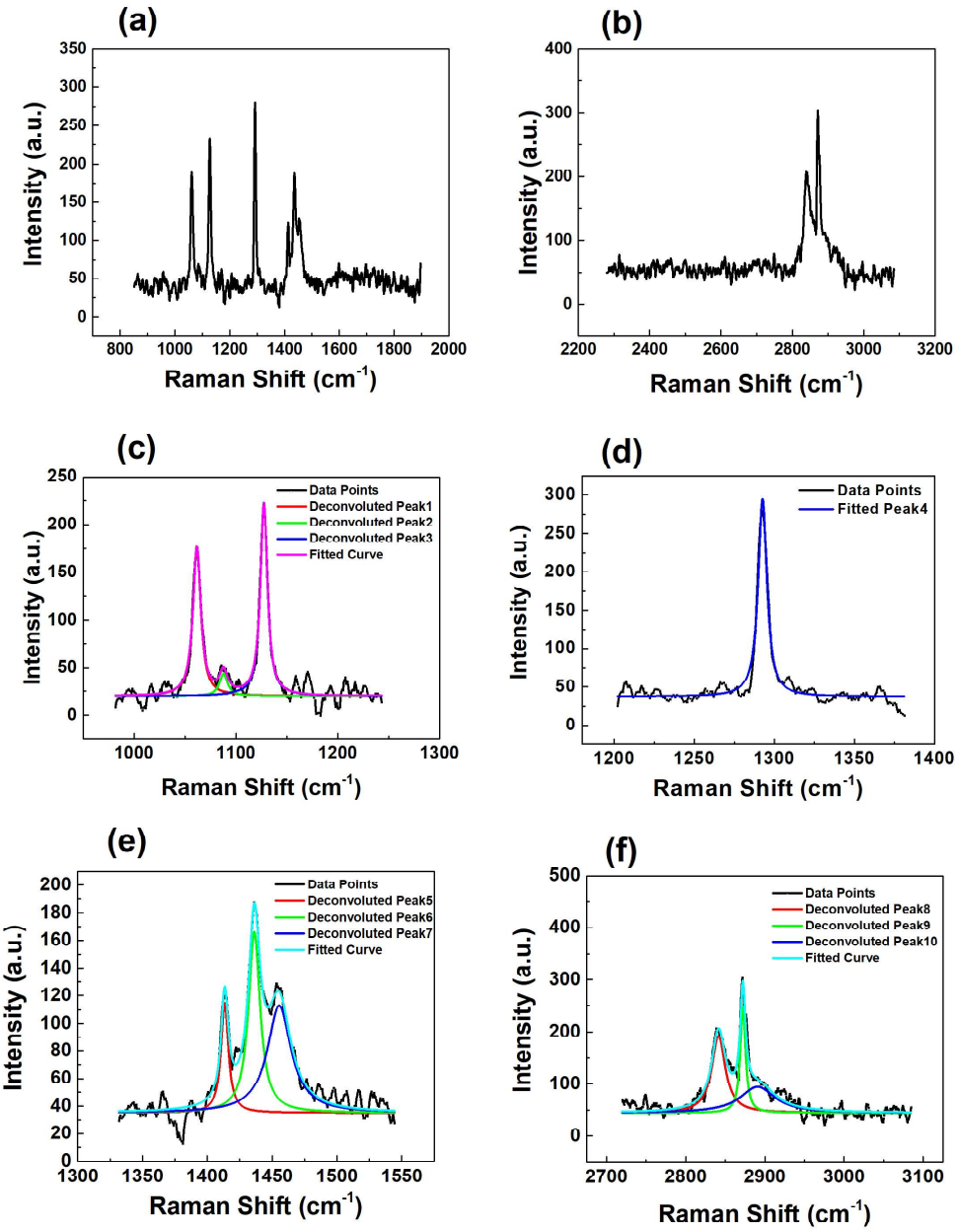

FIGURE 2.13: (a) Raman spectrum at room temperature for HDPE for a region varying from 850 cm^{-1} to 1900 cm^{-1} and (b) for a region of CH- Stretching mode between 2300 cm^{-1} to 3100 cm^{-1}. (a) and (b) spectrum collected for the same sample with different gratings of spectral resolution 0.925 cm^{-1} and 0.86 cm^{-1} respectively. (c) represents deconvolution of three closely appearing peaks between 1000 cm^{-1} to 1200 cm^{-1} into peaks 1, 2, and 3 (d) represents peak 4 at 1292 cm^{-1} (e) represents deconvoluted peaks 5, 6 and 7 between 1350 cm^{-1} to 1550 $^{-1}$ and (f) represents deconvolution of Raman band between 2800 cm^{-1} to 3100 cm^{-1} into peaks 8, 9 and 10. All the peaks fitted well with the Lorentzian function.

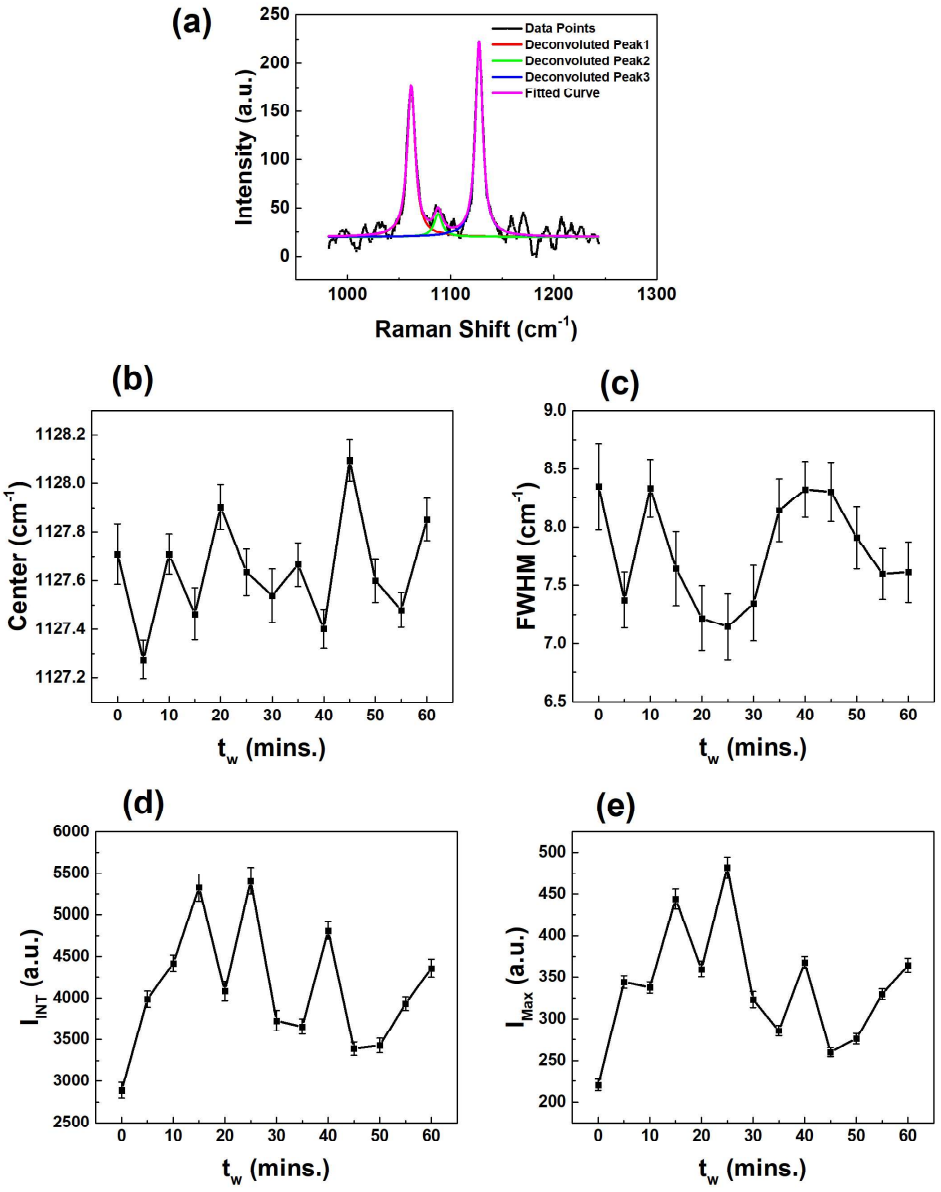

FIGURE 2.14: (a) The Raman band appearing between 1000 cm^{-1} to 1200 cm^{-1} for HDPE film is deconvoluted into three peaks: peaks 1, 2, and 3 using the Lorentzian function. (b), (c), (d), and (e) show respectively the time evolution of the peak center, the full width at half maxima (FWHM) of the peak, the integrated peak intensity or the area under the peak (I_{INT}) and the maximum peak intensity (I_{Max}) for peak 3 corresponding to C-C stretching mode present in the main chain of the polymer.

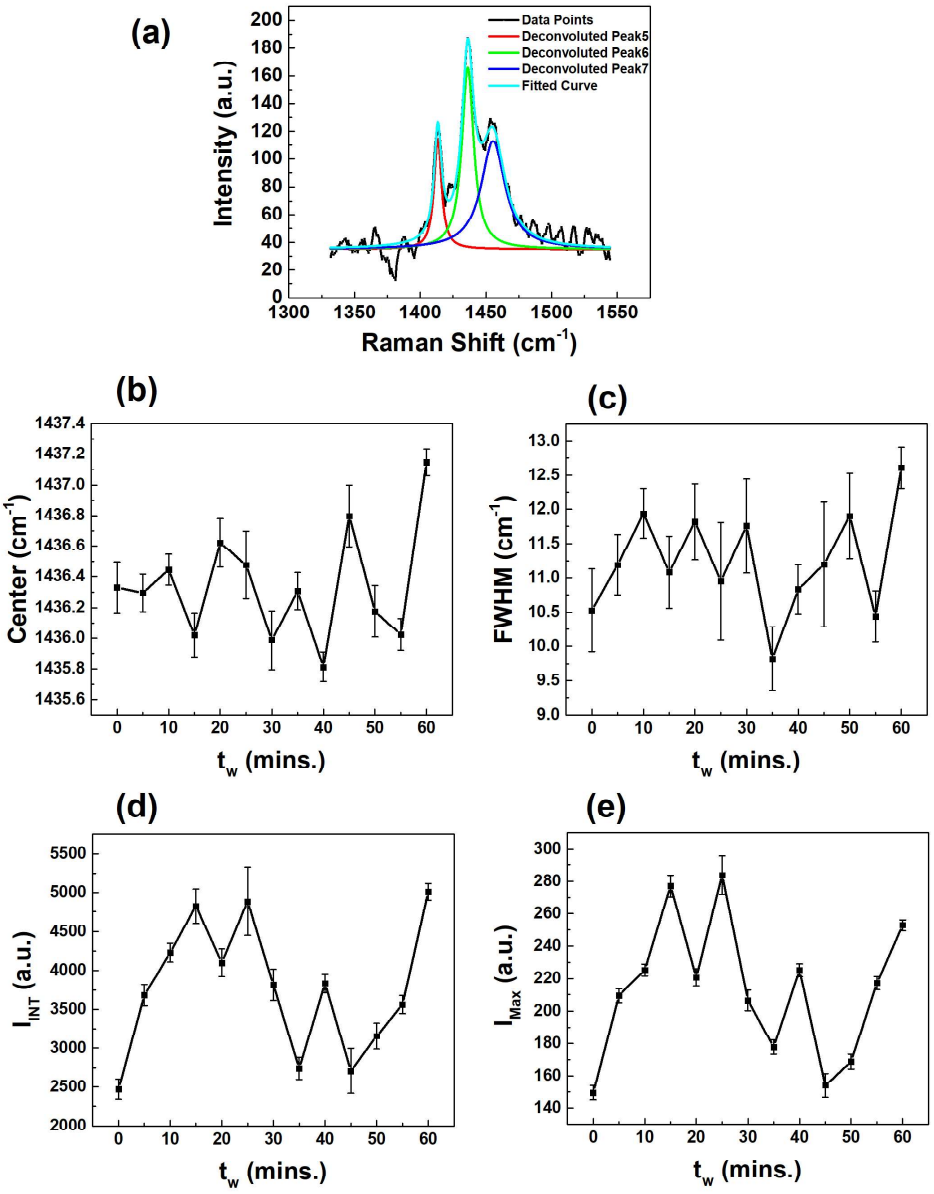

FIGURE 2.15: (a) The Raman band appearing between 1350 cm^{-1} to 1550 cm^{-1} for HDPE film is deconvoluted into three peaks: peaks 5, 6 and 7 using Lorentzian function. (b), (c), (d), and (e) show respectively the time evolution of the peak center, the full width at half maxima (FWHM) of the peak, the integrated peak intensity or the area under the peak (I_{INT}) and the maximum peak intensity (I_{Max}) for peak 5 corresponding to CH_2 scissoring mode present in the side chain of the polymer.

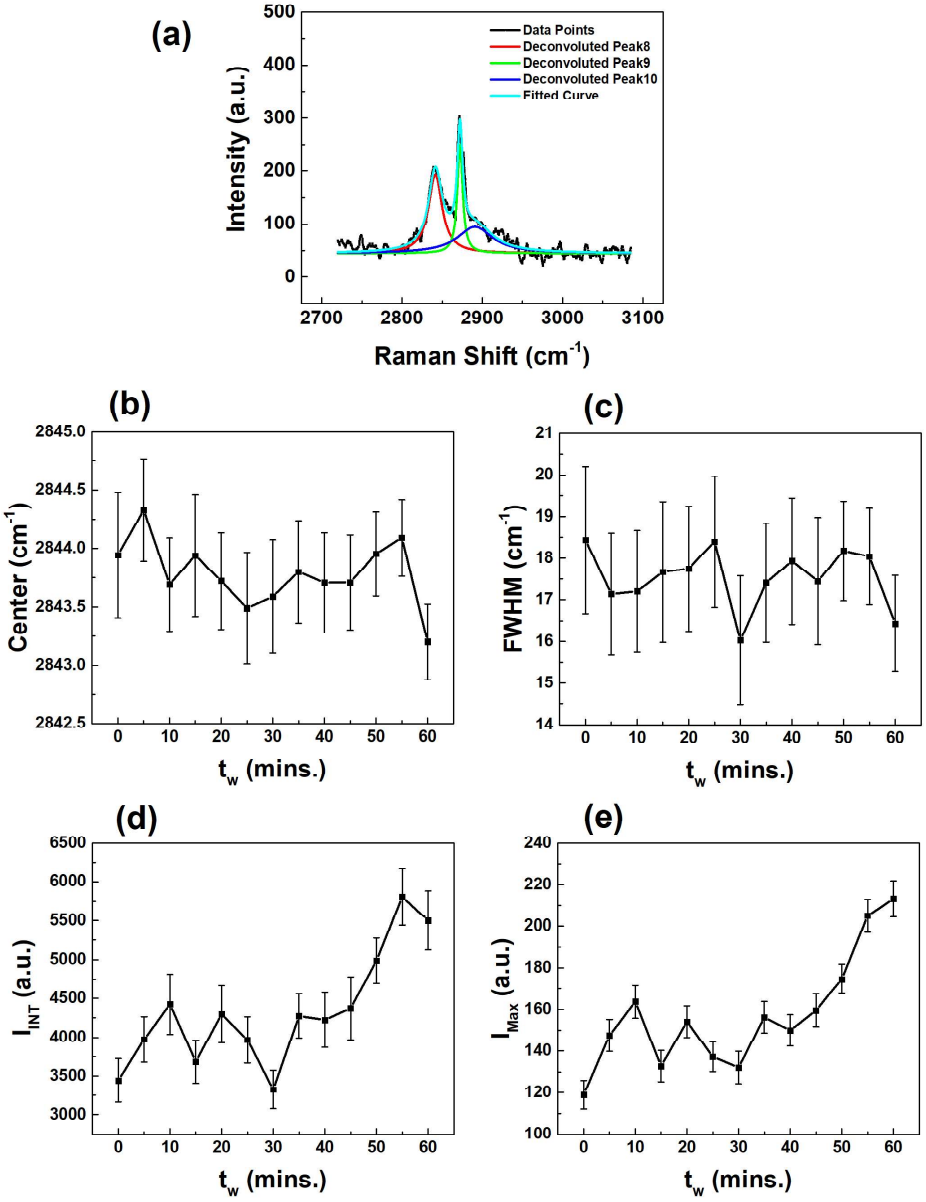

FIGURE 2.16: (a) The Raman band appearing between 2800 cm^{-1} to 3100 cm^{-1} for HDPE film is deconvoluted into three peaks: peaks 8, 9 and 10 using Lorentzian function. (b), (c), (d), and (e) show respectively the time evolution of the peak center, the full width at half maxima (FWHM) of the peak, the integrated peak intensity or the area under the peak (I_{INT}) and the maximum peak intensity (I_{Max}) for peak 8 corresponding to C-H stretching mode present in the main chain as well as side chain of the polymer.

HDPE, it is observed that in LLDPE the peaks are more intense as compared to HDPE.

To study the effect of the thermal perturbation on LLDPE film three peaks were chosen similar to HDPE i.e. peak 3 corresponding to C-C symmetric stretching mode present in the main chain of the polymer, peak 5 corresponding to CH_2 wagging mode present in the side chain of the polymer and peak 8 corresponding to C-H symmetric stretching mode present in both main chain and the side chain of the polymer. The C-C stretching mode (peak 3) of LLDPE film is shown in Figure 2.18(a). The peak center for peak 3 in LLDPE film (Figure 2.18(b)) shows a slight increase of 0.4 cm^{-1} with an increase in t_w and peak FWHM (Figure 2.18(c)) shows random fluctuation with a slight increase of 2.5 cm^{-1} after 30 minutes which again fluctuates with t_w. The I_{INT} (Figure 2.18(d)) and I_{Max} (Figure 2.18(e)) on the other hand show a strong decrease with increasing t_w with a dip at 40 and 45 minutes and then starts increasing with further increase in t_w.

For peak 5 (Figure 2.19(a)), the peak center shows random fluctuations with a variation of $\pm$ 0.4 cm^{-1} with an increase in t_w as shown in Figure 2.19(b). The FWHM on the other hand shows an increase of 4 cm^{-1} (Figure 2.19(c)) indicating an increase in random mobility of the polymer matrix. The I_{INT} (Figure 2.19(d)) and I_{Max} (Figure 2.19(e)) on the other hand show a characteristic similar to peak 3 with a decreasing character as a function of t_w having a minimum at 40 and 45 minutes respectively and then starts increasing with further increase in t_w.

The peak 8 (Figure 2.16(a)) of region 2 corresponding to C-H stretching modes shows a prominent decrease in peak center (Figure 2.16(b)) by 1.5 cm^{-1} whereas the FWHM (Figure 2.16(c)) shows random fluctuations as a function of t_w after the quench. The I_{INT} (Figure 2.20(d)) for peak 8 shows a character different from the other peaks with a slight decrease which is not prominent due to the presence of fluctuations.The I_{Max} (Figure 2.16(e)) shows prominent decrease with increase in t_w. However, an increase in I_{INT} and I_{Max} corresponds to an increase in the number of contributing molecules that are excited which is prominent in HDPE films, and a decrease in I_{INT} and I_{Max} indicates a decrease in the number of contributing molecules which is prominent in LLDPE films. This characteristic indicates that for LLDPE films there is less number of molecules contributing to the Raman spectrum which suggests that there is a higher amount of molecular mobility induced due to thermal perturbation in

LLDPE films which is also supported by the increase in FWHM.

2.7 Effect of change in temperature

To study the effect of change in temperature during thermal perturbation on the polymer films, the Raman peak intensity (I_{Max}) at three points of different temperature during the thermal quench cycle are analyzed: at RT, at T_{Max} and at T_{hold} as shown in Figure 2.21(a). Three vibrational modes are chosen to observe the effect of thermal perturbation at the molecular scale of polymers – C-C stretching from the main chain of the polymers, CH_2 scissoring from the side branch of the polymers, and C-H stretching which is present in both in the main chain and side branch of the polymer which are same as discussed in section 2.6 where the time evolution of the Raman peak parameters was compared.

The effect of temperature change on the peak intensity (I_{Max}) for PPC, HDPE, and LLDPE is shown in Figure 2.21(b). For PPC, HDPE and LLDPE, there is minimal change in I_{Max} of the C-H stretching modes which are present in both the main chain and side chain of the polymers, but a significant change in the C-C stretching modes which forms the backbone of the polymer structure. For HDPE and PPC I_{Max} of C-C stretching continuously increases which represents an increase in the number of modes contributing to the peak with increasing temperature and with rapid cooling. In LLDPE I_{Max} of C-C stretching mode decreases with increasing temperature. The CH_2 scissoring mode shows no substantial change with temperature in HDPE and PPC but in LLDPE I_{Max} decreases with increasing temperature and an increase in I_{Max} with decreasing temperature. This difference in the thermal response of PPC, HDPE, and LLDPE is due to their structure which helps in exciting a greater number of modes which results in higher peak intensity of Raman modes. I_{Max}

The variation in Raman peak intensity of different vibrational modes provides rich information about the variations in polymer chain conformations which can provide information about the amorphous and crystalline domains in the polymers [74]. Various methods have previously been employed to estimate crystallinity from Raman spectroscopy with the help of the ratio of Raman peak intensities [75, 76, 77, 78]. We have used the method employed by Ashok Samuel [77] from the ratio of a cross-section of crystalline and amorphous Raman peaks. The peak corresponding to the crystalline phase (trans-Raman mode) and

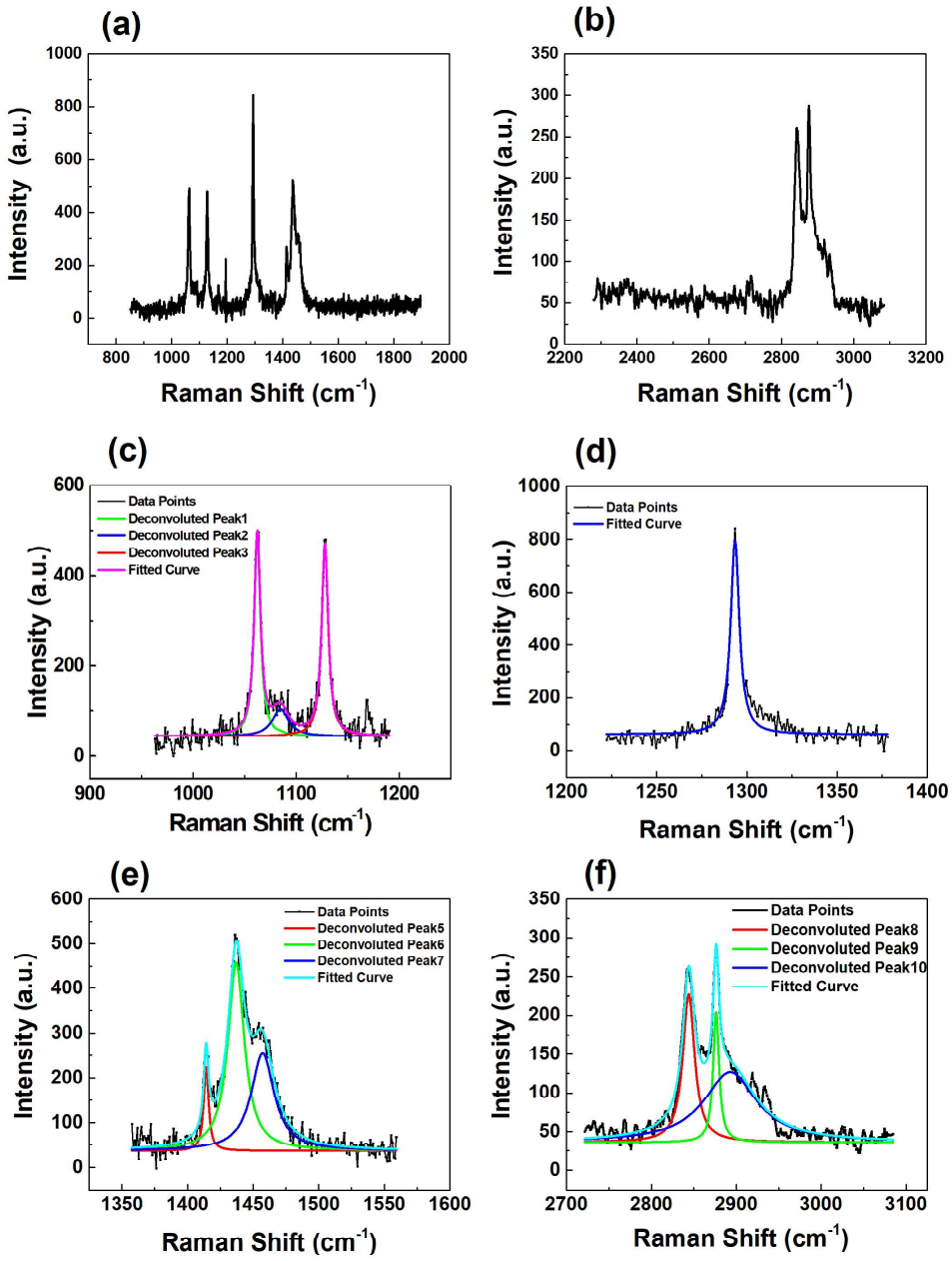

FIGURE 2.17: (a) Raman spectrum at room temperature for LLDPE for a region varying from 850 cm^{-1} to 1900 cm^{-1} and (b) for a region of CH- Stretching mode between 2300 cm^{-1} to 3100 cm^{-1}. (a) and (b) spectrum collected for the same sample with different gratings of spectral resolution 0.925 cm^{-1} and 0.86 cm^{-1} respectively. (c) represents deconvolution of three closely appearing peaks between 1000 cm^{-1} to 1200 cm^{-1} into peaks 1, 2, and 3 (d) represents peak 4 at 1292 cm^{-1} (e) represents deconvoluted peaks 5, 6 and 7 between 1350 cm^{-1} to 1550 $^{-1}$ and (f) represents deconvolution of Raman band between 2800 cm^{-1} to 3100 cm^{-1} into peaks 8, 9 and 10. All the peaks fitted well with the Lorentzian function.

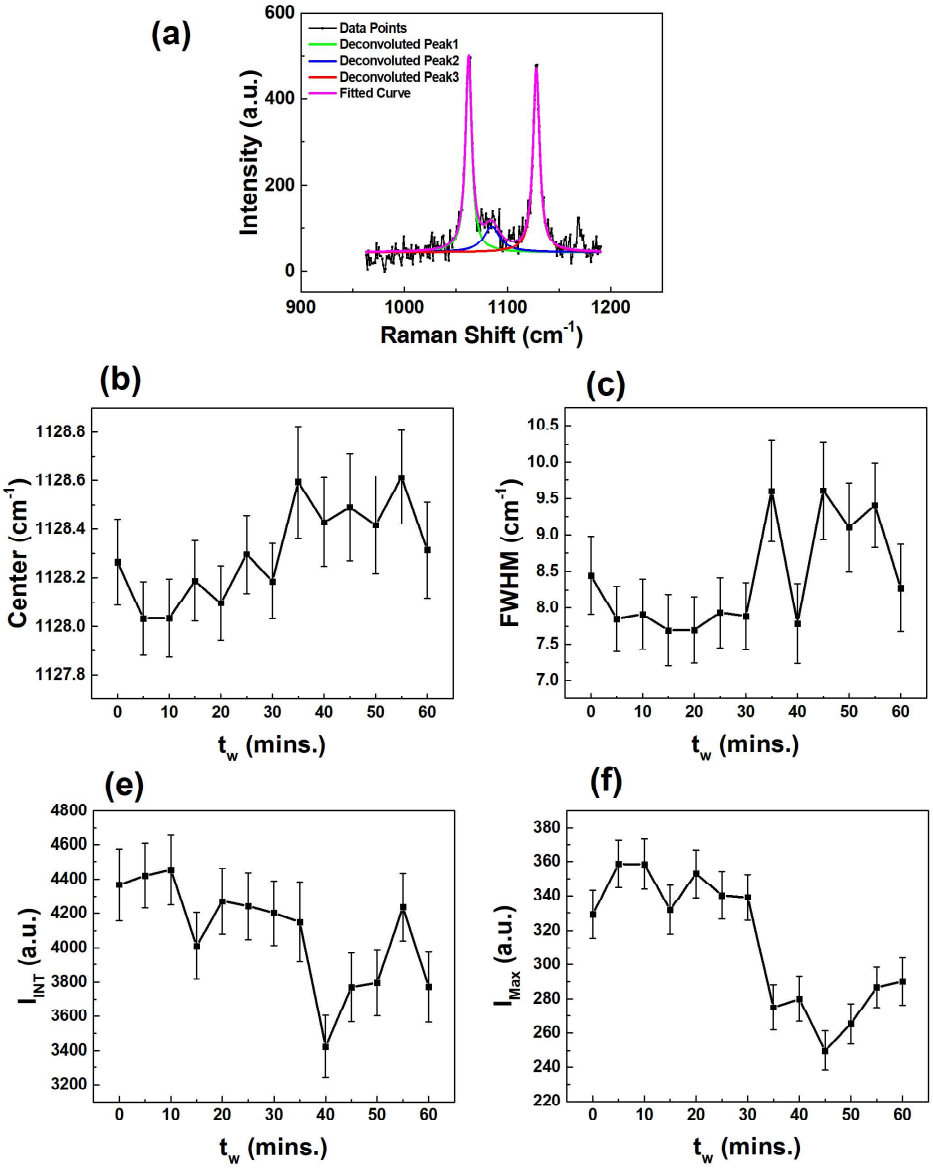

FIGURE 2.18: (a) The Raman band appearing between 1000 cm^{-1} to 1200 cm^{-1} for LLDPE film is deconvoluted into three peaks: peaks 1, 2, and 3 using the Lorentzian function. (b), (c), (d), and (e) show respectively the time evolution of the peak center, the full width at half maxima (FWHM) of the peak, the integrated peak intensity or the area under the peak (I_{INT}) and the maximum peak intensity (I_{Max}) for peak 3 corresponding to C-C stretching mode present in the main chain of the polymer.

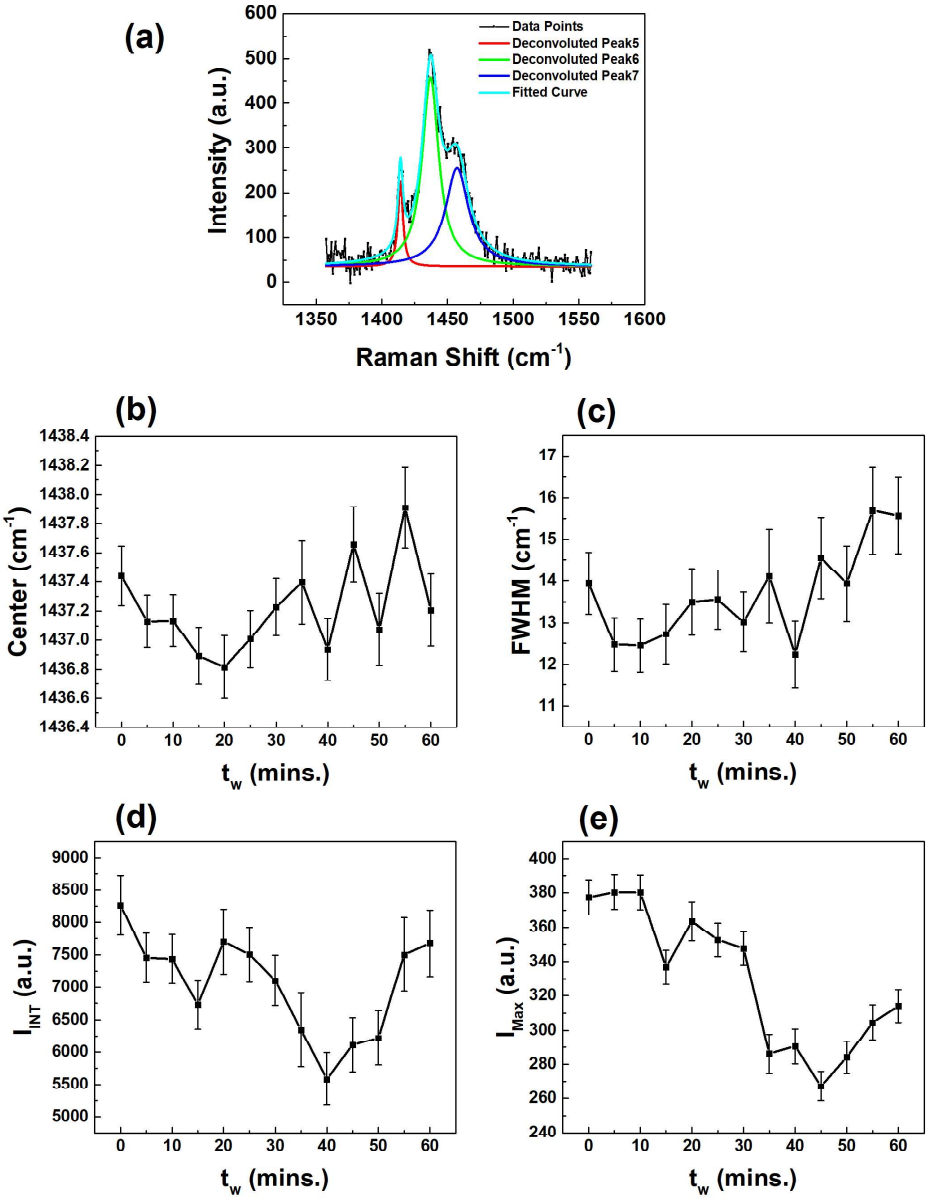

FIGURE 2.19: (a) The Raman band appearing between 1350 cm^{-1} to 1550 cm^{-1} for LLDPE film is deconvoluted into three peaks: peaks 5, 6 and 7 using Lorentzian function. (b), (c), (d), and (e) show respectively the time evolution of the peak center, the full width at half maxima (FWHM) of the peak, the integrated peak intensity or the area under the peak (I_{INT}) and the maximum peak intensity (I_{Max}) for peak 5 corresponding to CH_2 scissoring mode present in the side chain of the polymer.

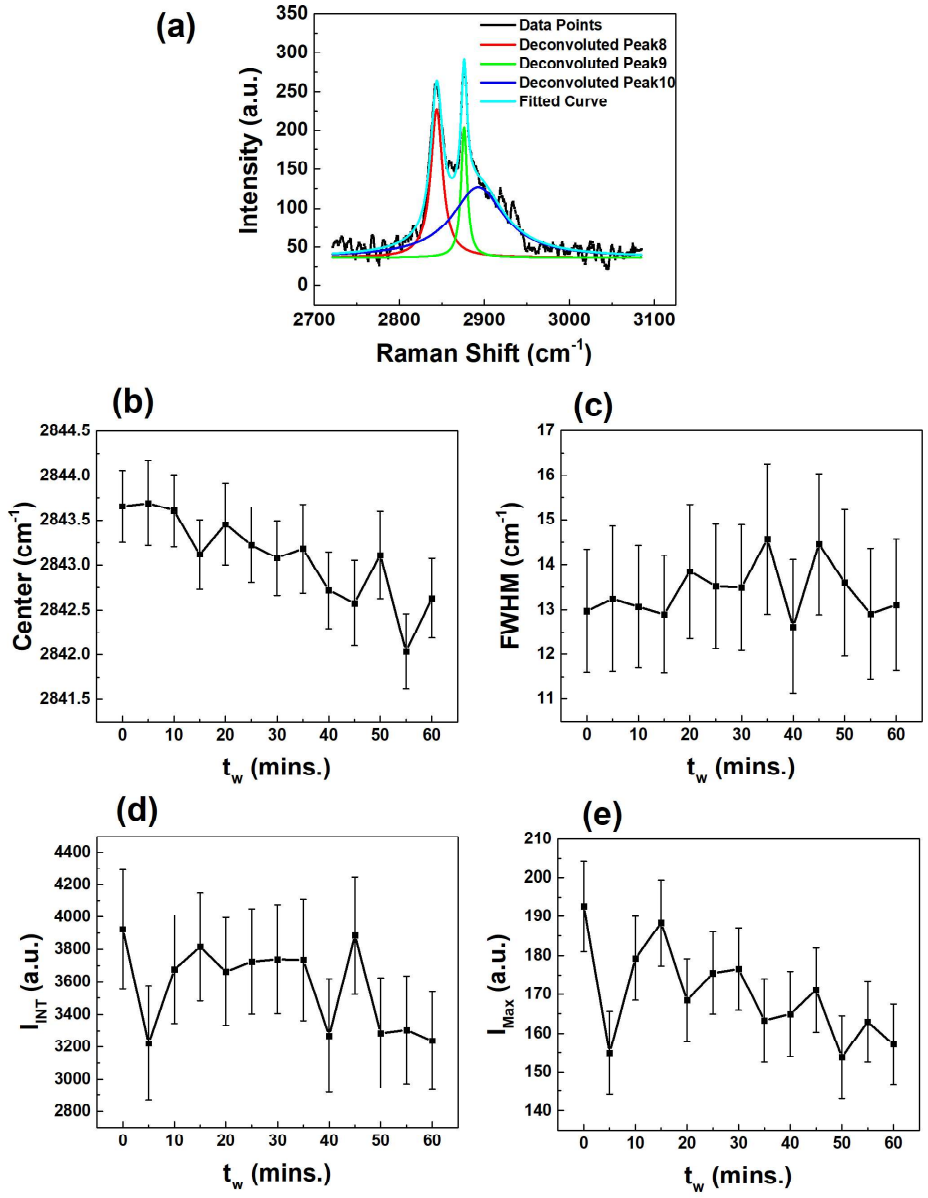

FIGURE 2.20: (a) The Raman band appearing between 2800 cm^{-1} to 3100 cm^{-1} for LLDPE film is deconvoluted into three peaks: peaks 8, 9 and 10 using Lorentzian function. (b), (c), (d), and (e) show respectively the time evolution of the peak center, the full width at half maxima (FWHM) of the peak, the integrated peak intensity or the area under the peak (I_{INT}) and the maximum peak intensity (I_{Max}) for peak 8 corresponding to C-H stretching mode present in the main chain as well as side chain of the polymer.

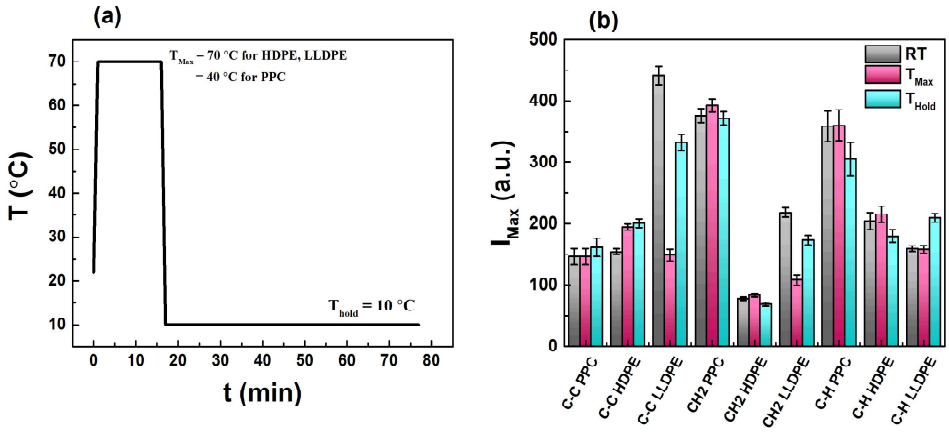

FIGURE 2.21: (a)Thermal quench applied to the polymer films, the temperature is increased from room temperature (RT=22 °C) to T_{Max} = 70 °C for HDPE and LLDPE and T_{Max} = 40 °C for PPC with a rate of 20 °C/min, after 15 minutes the temperature is quenched and maintained at T_{hold} = 10 °C with a rate of 60 °C/min. (b) Maximum Raman intensity I_{Max} at RT, T_{Max} and T_{hold} for the prominent vibrational modes discussed in section 2.6 are shown in the form of a bar graph.

amorphous phase (gauge Raman mode) of HDPE and LLDPE were found at 1080 and 1300 cm^{-1} respectively. The percentage crystallinity (PC) was calculated from the intensity of the trans (I_T) and gauge (I_G) vibrational modes from the following formula:

$$PC = \frac{I_G}{I_T + \zeta_{\frac{T}{G}} I_G} \tag{2.8}$$

where,

$$\zeta_{\frac{T}{G}} = \frac{\triangle I_T}{\triangle I_G} \tag{2.9}$$

It can be observed that with the increase in temperature, there is an increase in the PC of both HDPE and LLDPE, and with a sudden decrease in temperature, the PC decreases. After the thermal perturbation, when the polymers are maintained at a constant temperature, the PC fluctuates as a function of time. At room temperature, the PC of HDPE is 60% and PC of LLDPE is 37% (Figure 2.22), the difference in crystallinity is due to the branched structure of LLDPE which makes it more amorphous. On increasing the

temperature, PC increases indicating growth of the crystalline domain, and a network of crystallinity grows as shown in Figure 2.22. Similar results have been observed by Doumeng et. al. during the annealing of polyethylene films [79]. On decreasing the temperature, the PC of both HDPE and LLDPE first decreases and became comparable to each other, then fluctuates as a function of t_w. This indicates that even though the polymers are not driven in their glassy state, a small temperature change can influence the crystalline and amorphous domains present within the films. NMR studies by Cristian et.al. show that temperature change has a greater impact on the amorphous phase than the crystalline phase of the polymer and this induces molecular mobility in polymer films [80]. Therefore, if a thermal perturbation or a temperature change can affect the PC of the polymer, then it can also affect the macroscopic mechanical response of the polymer which is majorly dependent on the presence of crystalline and amorphous domains in the polymer. It has also been observed in several experiments where the change in temperature affects the mechanical properties of polymers [23, 37, 81]. Therefore, if a thermal perturbation can affect both the microscopic properties (like PC) and macroscopic properties (like tensile properties), then a correlation between the microscopic and macroscopic properties needs to be determined. Thus, it becomes important to study the correlation (if any) between changing PC or molecular mobility and the mechanical properties of the polymer. In this context, correlations between the results obtained from Raman spectroscopy and tensile testing were determined and discussed in the following section.

2.8 Correlation between vibrational and mechanical properties

The vibrational modes in the Raman spectrum provide information about the polymer chain conformations. Three modes representing the main chain and side branch of the polymers were selected to study the overall behavior of the polymer chain which includes the C-C stretching vibrations present in the main chain of the polymer, CH_2 scissoring vibrations present in the side chain of polymers, and C-H stretching vibrations present in both main chain and the side chain of the polymers. Apart from the polymer chain conformations, the

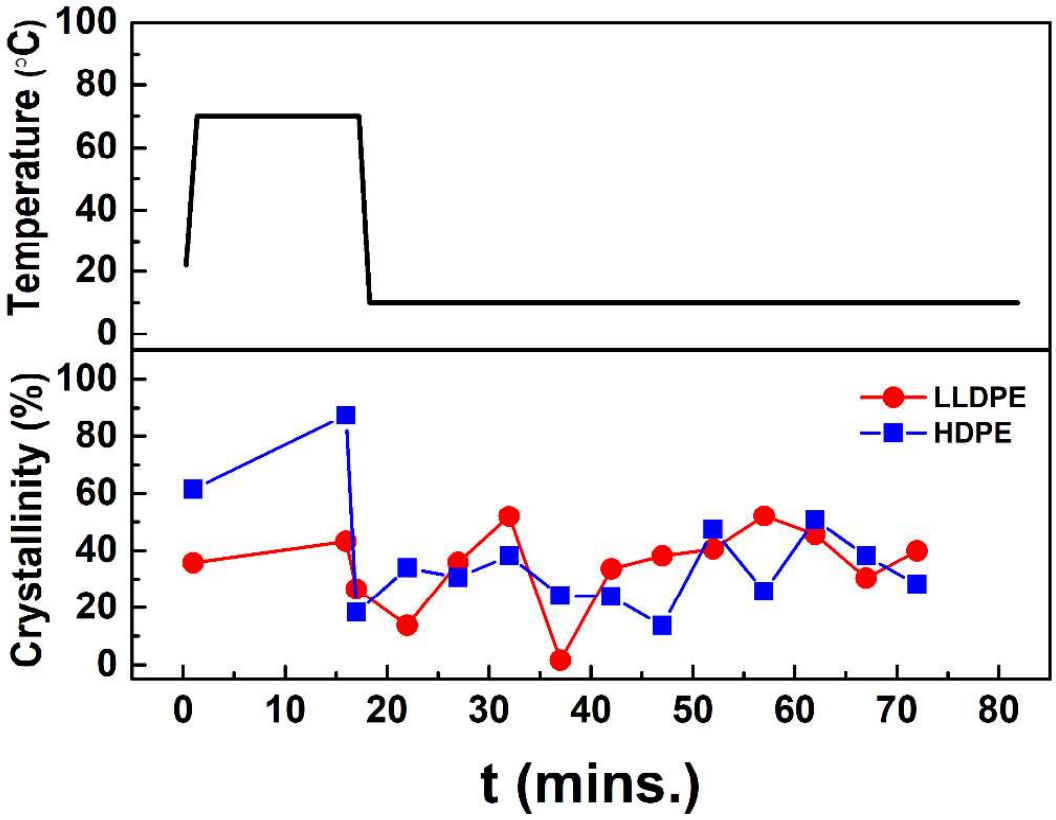

FIGURE 2.22: Variation in percentage crystallinity of HDPE (blue) and LLDPE (red) as a function of time due to the thermal cycle applied to the polymer films. The black schematic in layer 1 represents the thermal cycle applied to the polymer films and layer 2 shows the change in crystallinity as a function of temperature and time.

molecular vibrational modes obtained in the Raman spectrum also contain information about the mechanical properties of the polymer.

In context to the harmonic oscillator approximation, as discussed in section 2.5, the vibrational frequency of the Raman band depends on the reduced mass of the system (μ) and the spring constant k of the system which is shown in Equation 2.5. From Equation 2.5 the correlation between mechanical properties and Raman peak parameters was determined which is represented in terms of Pearson's correlation coefficients in Figure 2.23(a) for C-C stretching mode and Figure 2.23(b) for C-H stretching mode. The peak center for the C-C stretching mode is strongly correlated with Young's modulus (YM) and tensile strength (TS) where it is anti-correlated with the yield point (YP) of the polymer film. Peak area and FWHM on the other hand are anticorrelated with YM and TS and strongly correlated with YP. The peak height shows negligible correlation with the mechanical properties for the C-C stretching mode. The C-C stretching mode which builds the main chain of the polymer is a major contributor to the stiffness of the polymer chain. A strong correlation of the peak center of C-C stretching mode with the tensile properties is in agreement with Equation 2.5, indicating that any change in peak center will be reflected in the overall mechanical properties of the polymer. For the C-H stretching mode, this behavior is reversed where the YM and TS are negatively correlated with peak center, height, and area whereas strongly correlated with YP, indicating that the C-H stretching modes which are present in both the main chain and side branch of the polymer form a basis for the yielding of the polymer film. Any variation in the C-H stretching vibrations can therefore be accountable for the early or delayed yielding of the polymer films.

This illustrates a strong possibility that the macroscopic mechanical response of the material originates from the molecular scale vibrational transitions which subsequently govern the tensile properties of the polymer films. Therefore, any variation at the molecular level of the polymer will be reflected in the macroscopic mechanical properties of the polymer. It has often been observed that the mechanical response is affected by the molecular interactions [2], and several composites are also developed to enhance the mechanical properties of the polymer by changing the molecular orientation of the polymer [12]. One way to alter the molecular orientation is by changing the polymer processing or casting technique. A recent study by Mohammad et. al. has observed a

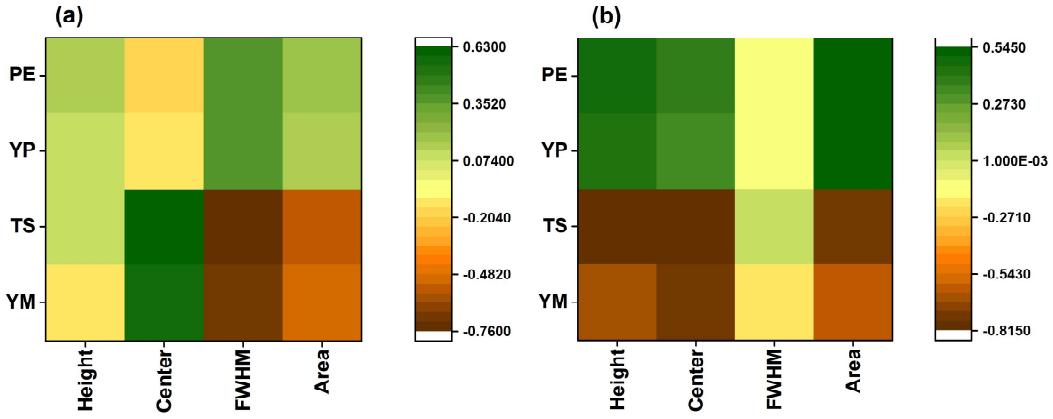

FIGURE 2.23: Correlation matrix of Pearson's correlation coefficients between Raman peak parameters and Young's modulus (YM), tensile strength (TS) and yield point (YP) of polymer films for (a) C-C stretching vibrational mode and (b) C-H stretching vibrational mode.

significant effect on the tensile response of HDPE films prepared from two different processing techniques [37]. Therefore, it is important to study the effect of processing techniques at the microscopic level to understand the variation in macroscopic properties for different processing techniques.

2.9 Effect of processing techniques

During applications of polymers, they are exposed to different processing techniques depending on the requirement of the end product. These processing techniques are known to affect the electrical as well as mechanical properties of the polymer products [82]. To study the effect of processing techniques on the molecular scale vibrational properties of polymers, HDPE films prepared from two different techniques: melt processing and drop casting were studied using Raman spectroscopy. Both the films were exposed to a thermal quench as shown in Figure 2.8 and the comparative variation in the I_{Max} and I_{INT} was analyzed by calculating the relative differential change in I_{Max} and I_{INT} as ϕ_H and ϕ_A respectively which can be represented as:

$$\phi_H = \frac{I_T - I_o(t_w)}{I_T} \tag{2.10}$$

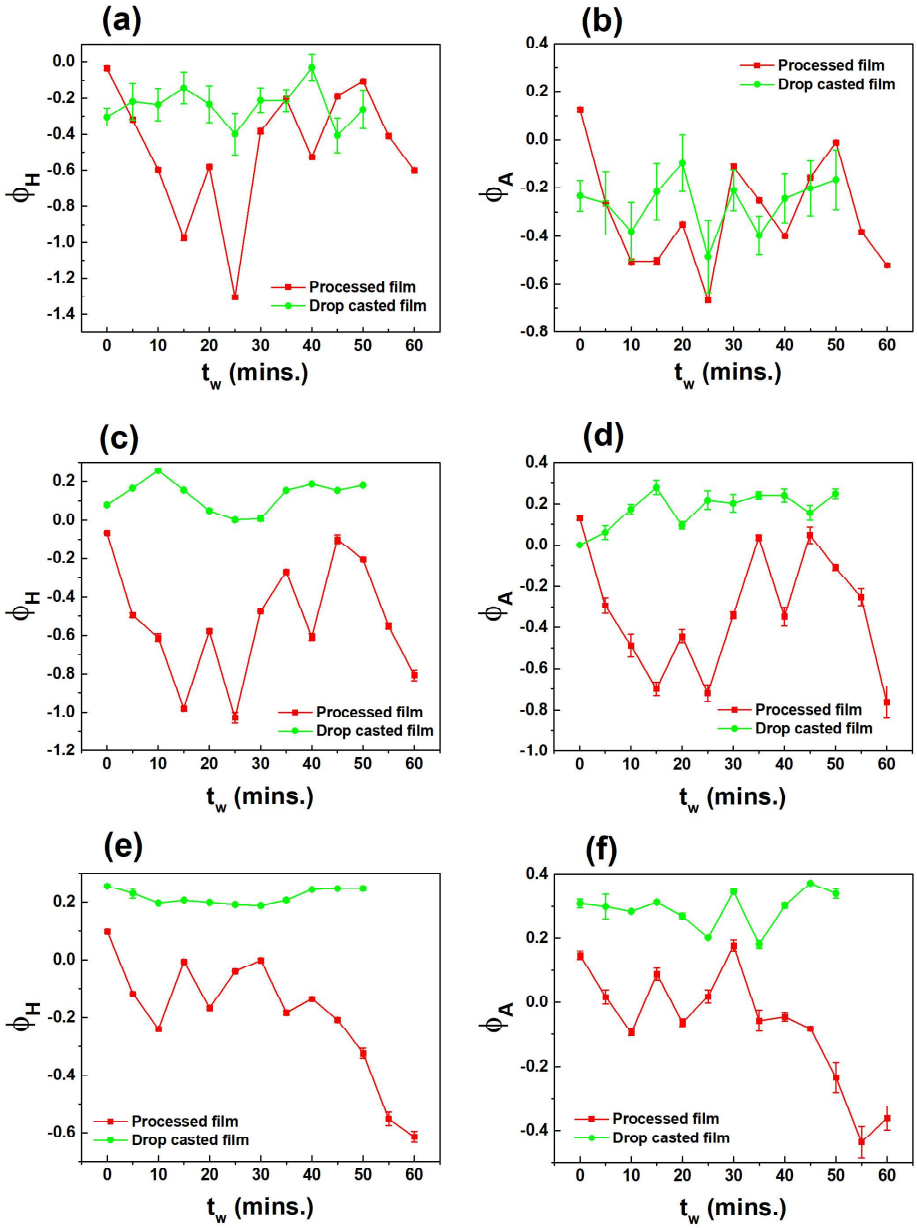

FIGURE 2.24: Relative differential change in I_{Max} and I_{INT} as ϕ_H and ϕ_A respectively for C-C stretching mode (a) and (b), CH_2 scissoring mode (c) and (d) and C-H stretching mode (e) and (f) for the processed and drop casted films of HDPE

where, I_T is I_{Max} at T_{Max} and $I_o(t_w)$ is I_{Max} as a function of waiting time after quench (t_w). Similarly,

$$\phi_A = \frac{A_T - A_o(t_w)}{A_T} \tag{2.11}$$

where, A_T is I_{INT} at T_{Max} and $A_o(t_w)$ is I_{INT} as a function of waiting time after quench.

The variation of ϕ_H and ϕ_A as a function of t_w is shown in Figure 2.24. Three Raman modes are represented in Figure 2.24 i.e. the C-C stretching, CH_2 scissoring, and the C-H stretching mode. For C-C stretching mode, the ϕ_H shows a prominent variation for the processed film but the drop casted film shows a very small change as a function of t_w (Figure 2.24(a)) whereas ϕ_A (Figure 2.24(b)) for both processed and drop casted films fluctuate within the same range. The ϕ_H (Figure 2.24(c)) and ϕ_A (Figure 2.24(d)) for CH_2 scissoring mode show similar characteristics where the drop casted film has minimal change, but the processed film has a large variation with t_w. The C-H stretching mode shows a similar behavior to CH_2 scissoring mode with a slight variation in ϕ_H (Figure 2.24(e)) and ϕ_A (Figure 2.24(f)) for the drop casted film and a large decreasing character for the processed film. It can therefore be stated that the processing technique affects the molecular vibrations in the polymer which can affect the molecular mobility and crystallinity within the polymer film which can ultimately affect the macroscopic properties of the polymer film. Therefore, for better applicability of any polymer, it is important to study not only the macroscopic properties but also the microscopic and molecular scale properties of the polymer.

2.10 Summary

The drop casted films of PPC showed good mechanical properties which were comparable to the traditional petroleum based polymers like HDPE and LLDPE and also with other synthetic polymer. Although PPC is mechanically strong but the glass transition temperature of PPC is close to room temperature. Therefore, the thermal stability of polymer needs to be thoroughly analyzed when developing suitable applications. The present Raman scattering study reveals that thermal perturbation has a large effect on the molecular mobility of PPC

chains, evident from FWHM changes. The reason for this is the proximity of the measurement temperature to the glass transition temperature of PPC. Even though HDPE and LLDPE were far from the glassy state, still the variation in molecular mobility was evident for a small thermal quench. The effect of processing techniques was also investigated, where a greater impact of thermal perturbations was observed for the processed HDPE films as compared to the drop-casted HDPE films. The molecular mobility and the contribution of vibrational modes to the Raman spectrum is higher in PPC as compared to processed HDPE and LLDPE films. Also, Young's modulus, tensile strength, and elongation at break for PPC are comparable to HDPE, LLDPE, and also to other non-biodegradable polymers existing in the polymer industry. Recently, other biodegradable polymers like polylactic acid (PLA) and its derivatives, polycaprolactone (PCL), polyhydroxy butyrate (PHB) and other natural fibers are also studied having high mechanical strength and glass transition temperature comparable to polyethylene which can be used for sustainable applications [11, 83]. The enhancement of mechanical properties and thermal stability of biodegradable polymers by developing polymer nanocomposites for potential applications should therefore be explored.

Refernces

[1] Md Hafizur Rahman and Prakashbhai R Bhoi. An overview of non-biodegradable bioplastics. *Journal of cleaner production*, 294:126218, 2021.

[2] Yusheng Qin, Lijie Chen, Xianhong Wang, Xiaojiang Zhao, and Fosong Wang. Enhanced mechanical performance of poly (propylene carbonate) via hydrogen bonding interaction with o-lauroyl chitosan. *Carbohydrate polymers*, 84(1):329–334, 2011.

[3] Sergi Montava-Jordà, Sergio Torres-Giner, Santiago Ferrandiz-Bou, Luis Quiles-Carrillo, and Nestor Montanes. Development of sustainable and cost-competitive injection-molded pieces of partially bio-based polyethylene terephthalate through the valorization of cotton textile waste. *International Journal of Molecular Sciences*, 20(6):1378, 2019.

[4] Guo Jiang, Jian Feng, Mengdi Zhang, Shuidong Zhang, and Hanxiong Huang. Structure, and thermal and mechanical properties of poly (propylene carbonate) capped with different types of acid anhydride via reactive extrusion. *RSC advances*, 6(109):107547–107555, 2016.

[5] Valentina Siracusa and Ignazio Blanco. Bio-polyethylene (bio-pe), bio-polypropylene (bio-pp) and bio-poly (ethylene terephthalate)(bio-pet): Recent developments in bio-based polymers analogous to petroleum-derived ones for packaging and engineering applications. *Polymers*, 12(8):1641, 2020.

[6] M Sai Bhargava Reddy, Deepalekshmi Ponnamma, Rajan Choudhary, and Kishor Kumar Sadasivuni. A comparative review of natural and synthetic biopolymer composite scaffolds. *Polymers*, 13(7):1105, 2021.

[7] Mohammad Ali Tavanaie and Amir Hossein Ghahari. A study on melt recycling of bio-based polypropylene/thermoplastic starch compound. *Journal of Applied Polymer Science*, 138(43):51282, 2021.

[8] William R Newson, Faiza Rasheed, Ramune Kuktaite, Mikael S Hedenqvist, Mikael Gällstedt, Tomás S Plivelic, and Eva Johansson. Commercial potato protein concentrate as a novel source for thermoformed bio-based plastic films with unusual polymerisation and tensile properties. *Rsc Advances*, 5(41):32217–32226, 2015.

[9] Rowen Lim, Peck Loo Kiew, Man Kee Lam, Wei Ming Yeoh, and Mui Yen Ho. Corn starch/pva bioplastics—the properties and biodegradability study using chlorella vulgaris cultivation. *Asia-Pacific Journal of Chemical Engineering*, 16(3):e2622, 2021.

[10] C Valeria L Giosafatto, Asmaa Al-Asmar, Antonio D'Angelo, Valentina Roviello, Marilena Esposito, and Loredana Mariniello. Preparation and characterization of bioplastics from grass pea flour cast in the presence of microbial transglutaminase. *Coatings*, 8(12):435, 2018.

[11] Xipo Zhao, Huan Hu, Xin Wang, Xiaolei Yu, Weiyi Zhou, and Shaoxian Peng. Super tough poly (lactic acid) blends: A comprehensive review. *RSC Advances*, 10(22):13316–13368, 2020.

[12] Yichen Guo, Shan He, Kai Yang, Yuan Xue, Xianghao Zuo, Yingjie Yu, Ying Liu, Chung-Chueh Chang, and Miriam H Rafailovich. Enhancing the mechanical properties of biodegradable polymer blends using tubular nanoparticle stitching of the interfaces. *ACS applied materials & interfaces*, 8(27):17565–17573, 2016.

[13] I Taha and G Ziegmann. A comparison of mechanical properties of natural fiber filled biodegradable and polyolefin polymers. *Journal of composite materials*, 40(21):1933–1946, 2006.

[14] Yonghang Xu, Limiao Lin, Min Xiao, Shuanjin Wang, Andrew T Smith, Luyi Sun, and Yuezhong Meng. Synthesis and properties of co2-based plastics: Environmentally-friendly, energy-saving and biomedical polymeric materials. *Progress in Polymer Science*, 80:163–182, 2018.

[15] SJ Wang, LC Du, XS Zhao, YZ Meng, and SC Tjong. Synthesis and characterization of alternating copolymer from carbon dioxide and propylene oxide. *Journal of applied polymer science*, 85(11):2327–2334, 2002.

[16] Dongmei Han, Zhen Guo, Shou Chen, Min Xiao, Xiaohua Peng, Shuanjin Wang, and Yuezhong Meng. Enhanced properties of biodegradable poly (propylene carbonate)/polyvinyl formal blends by melting compounding. *Polymers*, 10(7):771, 2018.

[17] GJ Chen, YY Wang, SJ Wang, M Xiao, and YZ Meng. Orientation microstructure and properties of poly (propylene carbonate)/poly (butylene succinate) blend films. *Journal of applied polymer science*, 128(1):390–399, 2013.

[18] XL Lu, FG Du, XC Ge, M Xiao, and YZ Meng. Biodegradability and thermal stabilityof poly (propylene carbonate)/starch composites. *Journal of Biomedical Materials Research Part A: An Official Journal of The Society for Biomaterials, The Japanese Society for Biomaterials, and The Australian Society for Biomaterials and the Korean Society for Biomaterials*, 77(4):653–658, 2006.

[19] MZ Pang, JJ Qiao, J Jiao, SJ Wang, M Xiao, and YZ Meng. Miscibility and properties of completely biodegradable blends of poly (propylene carbonate) and poly (butylene succinate). *Journal of Applied Polymer Science*, 107(5):2854–2860, 2008.

[20] Natalia G Perez-De Eulate and Daniele Cangialosi. The very long-term physical aging of glassy polymers. *Physical Chemistry Chemical Physics*, 20(18):12356–12361, 2018.

[21] Leendert Cornelis Elisa Struik. Physical aging in plastics and other glassy materials. *Polymer Engineering & Science*, 17(3):165–173, 1977.

[22] JM Hutchinson, S Smith, B Horne, and GM Gourlay. Physical aging of polycarbonate: enthalpy relaxation, creep response, and yielding behavior. *Macromolecules*, 32(15):5046–5061, 1999.

[23] Leila Malekmotiei, George Z Voyiadjis, Aref Samadi-Dooki, Fengyuan Lu, and Jianren Zhou. Effect of annealing temperature on interrelation between the microstructural evolution and plastic deformation in polymers. *Journal of polymer science part B: Polymer Physics*, 55(17):1286–1297, 2017.

[24] D Cangialosi, H Schut, A Van Veen, and SJ Picken. Positron annihilation lifetime spectroscopy for measuring free volume during physical aging of polycarbonate. *Macromolecules*, 36(1):142–147, 2003.

[25] OA Hasan, MC Boyce, XS Li, and S Berko. An investigation of the yield and postyield behavior and corresponding structure of poly (methyl methacrylate). *Journal of polymer science part B: polymer physics*, 31(2):185–197, 1993.

[26] George Z Voyiadjis and Aref Samadi-Dooki. Constitutive modeling of large inelastic deformation of amorphous polymers: Free volume and shear transformation zone dynamics. *Journal of Applied Physics*, 119(22):225104, 2016.

[27] Joachim Rösler, Harald Harders, and Martin Bäker. *Mechanical behaviour of engineering materials: metals, ceramics, polymers, and composites*. Springer Science & Business Media, 2007.

[28] Yehia M Haddad and YM Haddad. *Mechanical Behaviour of Engineering Materials: Volume 1: Static and Quasi-Static Loading*. Springer, 2000.

[29] Andrzej Pawlak. Cavitation during deformation of polymers on the example of polypropylene. *Journal of applied polymer science*, 125(6):4177–4187, 2012.

[30] Pengfei Guan, Shuo Lu, Michael JB Spector, Pavan K Valavala, and Michael L Falk. Cavitation in amorphous solids. *Physical Review Letters*, 110(18):185502, 2013.

[31] Jörg Rottler and Mark O Robbins. Growth, microstructure, and failure of crazes in glassy polymers. *Physical Review E*, 68(1):011801, 2003.

[32] Kallol Paul, Ratul Dasgupta, Jürgen Horbach, and Smarajit Karmakar. Cavity formation in deformed amorphous solids on the nanoscale. *Physical Review Research*, 2(4):042012, 2020.

[33] Andrzej Pawlak and Andrzej Galeski. Plastic deformation of crystalline polymers: the role of cavitation and crystal plasticity. *Macromolecules*, 38(23):9688–9697, 2005.

[34] C G'sell and A Dahoun. Evolution of microstructure in semi-crystalline polymers under large plastic deformation. *Materials Science and Engineering: A*, 175(1-2):183–199, 1994.

[35] Z Bartczak, A Galeski, AS Argon, and RE Cohen. On the plastic deformation of the amorphous component in semicrystalline polymers. *Polymer*, 37(11):2113–2123, 1996.

[36] Wei Zou, Rongyuan Chen, Haichen Zhang, and Jinping Qu. Preparation, melting behavior and thermal stability of poly (lactic acid)/poly (propylene carbonate) blends processed by vane extruder. In *AIP Conference Proceedings*, volume 1713, page 050003. AIP Publishing LLC, 2016.

[37] Mohammad Amjadi and Ali Fatemi. Tensile behavior of high-density polyethylene including the effects of processing technique, thickness, temperature, and strain rate. *Polymers*, 12(9):1857, 2020.

[38] E Laredo, N Suarez, A Bello, and L Marquez. The glass transition in linear low density polyethylene determined by thermally stimulated depolarization currents. *Journal of Polymer Science Part B: Polymer Physics*, 34(4):641–648, 1996.

[39] Kyucheol Cho, Byung H Lee, Kyu-Myun Hwang, Hoseok Lee, and Soonja Choe. Rheological and mechanical properties in polyethylene blends. *Polymer Engineering & Science*, 38(12):1969–1975, 1998.

[40] AO Ogah and JN Afiukwa. The effect of linear low density polyethylene (lldpe) on the mechanical properties of high density polyethylene (hdpe) film blends. *Int J Eng Manag Sci*, 3(2):85–90, 2012.

[41] Neçar Merah, F Saghir, Z Khan, and Abdelaziz Bazoune. Effect of temperature on tensile properties of hdpe pipe material. *Plastics, rubber and composites*, 35(5):226–230, 2006.

[42] E Kontou and M Niaounakis. Thermo-mechanical properties of lldpe/sio2 nanocomposites. *Polymer*, 47(4):1267–1280, 2006.

[43] Ching Yern Chee, NL Song, Luqman Chuah Abdullah, Thomas SY Choong, Azowa Ibrahim, and TR Chantara. Characterization of mechanical properties: low-density polyethylene nanocomposite using nanoalumina particle as filler. *Journal of Nanomaterials*, 2012:118–118, 2012.

[44] Moustafa Mahmoud Yousry Mahmoud Zaghloul. Mechanical properties of linear low-density polyethylene fire-retarded with melamine polyphosphate. *Journal of Applied Polymer Science*, 135(46):46770, 2018.

[45] Erick Gabriel Ribeiro dos Anjos, Eduardo Henrique Backes, Juliano Marini, Luiz Antonio Pessan, Larissa Stieven Montagna, and Fabio Roberto Passador. Effect of lldpe-g-ma on the rheological, thermal, mechanical properties and morphological characteristic of pa6/lldpe blends. *Journal of Polymer Research*, 26:1–10, 2019.

[46] Tai Jin-hua, Liu Guo-qin, Caiyi Huang, and Shangguan Lin-jian. Mechanical properties and thermal behaviour of lldpe/mwnts nanocomposites. *Materials Research*, 15:1050–1056, 2012.

[47] I Krupa and AS Luyt. Mechanical properties of uncrosslinked and crosslinked linear low-density polyethylene/wax blends. *Journal of Applied Polymer Science*, 81(4):973–980, 2001.

[48] Rattikarn Khankrua, Sommai Pivsa-Art, Hamada Hiroyuki, and Supakij Suttiruengwong. Thermal and mechanical properties of biodegradable polyester/silica nanocomposites. *Energy Procedia*, 34:705–713, 2013.

[49] Yishan Fang, Jianxin Fu, Chunjing Tao, Pengfei Liu, and Bo Cui. Mechanical properties and antibacterial activities of novel starch-based composite films incorporated with salicylic acid. *International journal of biological macromolecules*, 155:1350–1358, 2020.

[50] Niyi Gideon Olaiya, Arif Nuryawan, Peter Kayode Oke, HPS Abdul Khalil, Samsul Rizal, PB Mogaji, ER Sadiku, SR Suprakas, Peter Kayode Farayibi, Vincent Ojijo, et al. The role of two-step blending in the properties of starch/chitin/polylactic acid biodegradable composites for biomedical applications. *Polymers*, 12(3):592, 2020.

[51] Jianchun Li, Yong He, and Yoshio Inoue. Thermal and mechanical properties of biodegradable blends of poly (l-lactic acid) and lignin. *Polymer International*, 52(6):949–955, 2003.

[52] Ji-Zhao Liang, De-Rong Duan, Chak-Yin Tang, Chi-Pong Tsui, and Da-Zhu Chen. Tensile properties of plla/pcl composites filled with nanometer calcium carbonate. *Polymer testing*, 32(3):617–621, 2013.

[53] Paresh Kumar Samantaray, Alastair Little, David M Haddleton, Tony McNally, Bowen Tan, Zhaoyang Sun, Weijie Huang, Yang Ji, and Chaoying Wan. Poly (glycolic acid)(pga): A versatile building block expanding high performance and sustainable bioplastic applications. *Green Chemistry*, 22(13):4055–4081, 2020.

[54] Hyoung-Joon Jin, Boo-Young Lee, Mal-Nam Kim, and Jin-San Yoon. Properties and biodegradation of poly (ethylene adipate) and poly (butylene succinate) containing styrene glycol units. *European polymer journal*, 36(12):2693–2698, 2000.

[55] Naozumi Teramoto, Yuichi Saitoh, Atsuo Takahashi, and Mitsuhiro Shibata. Biodegradable polyurethane elastomers prepared from isocyanate-terminated poly (ethylene adipate), castor oil, and glycerol. *Journal of applied polymer science*, 115(6):3199–3204, 2010.

[56] Thomas Dooher, Cormac McGarrigle, Dorian Dixon, Alistair McIlhagger, Eileen Harkin-Jones, and Edward Archer. Novel thermoplastic yarn for the through-thickness reinforcement of fibre-reinforced polymer composites. *Journal of Thermoplastic Composite Materials*, 31(12):1619–1633, 2018.

[57] Zhu Xiong, Xinyan Dai, Ruoyu Zhang, Zhaobin Tang, Haining Na, and Jin Zhu. Preparation of biobased monofunctional compatibilizer from cardanol to fabricate polylactide/starch blends with superior tensile properties. *Industrial & Engineering Chemistry Research*, 53(26):10653–10659, 2014.

[58] Yongjin Li and Hiroshi Shimizu. Compatibilization by homopolymer: Significant improvements in the modulus and tensile strength of ppc/pmma blends by the addition of a small amount of pvac. *ACS Applied Materials & Interfaces*, 1(8):1650–1655, 2009.

[59] Xiaofei Ma, Peter R Chang, Jiugao Yu, and Ning Wang. Preparation and properties of biodegradable poly (propylene carbonate)/thermoplastic dried starch composites. *Carbohydrate Polymers*, 71(2):229–234, 2008.

[60] Sazzadur Rahman, Achyut Konwar, Gitanjali Majumdar, and Devasish Chowdhury. Guar gum-chitosan composite film as excellent material for packaging application. *Carbohydrate Polymer Technologies and Applications*, 2:100158, 2021.

[61] Rouhollah Khodaeimehr, Seyed Jamaleddin Peighambardoust, and Seyed Hadi Peighambardoust. Preparation and characterization of corn starch/clay nanocomposite films: Effect of clay content and surface modification. *Starch-Stärke*, 70(3-4):1700251, 2018.

[62] Trina Ghosh Dastidar and Anil N Netravali. 'green'crosslinking of native starches with malonic acid and their properties. *Carbohydrate polymers*, 90(4):1620–1628, 2012.

[63] Teboho Clement Mokhena, Emmanuel Rotimi Sadiku, Mokgaotsa Jonas Mochane, Suprakas Sinha Ray, Maya Jacob John, and Asanda Mtibe. Mechanical properties of cellulose nanofibril papers and their bionanocomposites: A review. *Carbohydrate Polymers*, 273:118507, 2021.

[64] Eugene Enriquez, Amar Kumar Mohanty, and Manjusri Misra. Biobased polymer blends of poly (trimethylene terephthalate) and high density polyethylene. *Materials & Design*, 90:984–990, 2016.

[65] Itziar Otaegi, Nora Aramburu, Alejandro J Müller, and Gonzalo Guerrica-Echevarría. Novel biobased polyamide 410/polyamide 6/cnt nanocomposites. *Polymers*, 10(9):986, 2018.

[66] Robert A Riggleman, Hau-Nan Lee, MD Ediger, and Juan J De Pablo. Heterogeneous dynamics during deformation of a polymer glass. *Soft Matter*, 6(2):287–291, 2010.

[67] Hau-Nan Lee, Keewook Paeng, Stephen F Swallen, and MD Ediger. Direct measurement of molecular mobility in actively deformed polymer glasses. *Science*, 323(5911):231–234, 2009.

[68] Christopher L Soles, Adam B Burns, Kanae Ito, Edwin P Chan, Jack F Douglas, Jinhuang Wu, Albert F Yee, Yueh-Ting Shih, Liping Huang, Robert M Dimeo, et al. Why enhanced subnanosecond relaxations are important for toughness in polymer glasses. *Macromolecules*, 54(5):2518–2528, 2021.

[69] Douglas C Hofmann, Jin-Yoo Suh, Aaron Wiest, Gang Duan, Mary-Laura Lind, Marios D Demetriou, and William L Johnson. Designing metallic glass matrix composites with high toughness and tensile ductility. *Nature*, 451(7182):1085–1089, 2008.

[70] SM Fielding, ME Cates, and P Sollich. Shear banding, aging and noise dynamics in soft glassy materials. *Soft Matter*, 5(12):2378–2382, 2009.

[71] John M Chalmers and Peter R Griffiths. *Handbook of vibrational spectroscopy*. Wiley, 2002.

[72] Takumitsu Kida, Yusuke Hiejima, and Koh-hei Nitta. Raman spectroscopic study of high-density polyethylene during tensile deformation. *Int. J. Exp. Spectroscopic Tech*, 1(001), 2016.

[73] Yonghae Cho, Masamichi Kobayashi, and Hiroyuki Tadokoro. Raman band profiles and mobility of polymethylene chains. *The Journal of chemical physics*, 84(8):4636–4642, 1986.

[74] Ashok Zachariah Samuel and Siva Umapathy. Energy funneling and macromolecular conformational dynamics: a 2d raman correlation study of peg melting. *Polymer journal*, 46(6):330–336, 2014.

[75] GR Strobl and W Hagedorn. Raman spectroscopic method for determining the crystallinity of polyethylene. *Journal of Polymer Science: Polymer Physics Edition*, 16(7):1181–1193, 1978.

[76] Anders Steen Nielsen, DN Batchelder, and Ryszard Pyrz. Estimation of crystallinity of isotactic polypropylene using raman spectroscopy. *Polymer*, 43(9):2671–2676, 2002.

[77] Ashok Zachariah Samuel. Direct estimation of polymer crystallinity with raman spectroscopy using ratio of scattering cross-sections estimated from variable temperature measurements. *Spectrochimica Acta Part A: Molecular and Biomolecular Spectroscopy*, 224:117431, 2020.

[78] Ashok Zachariah Samuel, Bo-Han Lai, Shih-Ting Lan, Masahiro Ando, Chien-Lung Wang, and Hiro-o Hamaguchi. Estimating percent crystallinity of polyethylene as a function of temperature by raman spectroscopy multivariate curve resolution by alternating least squares. *Analytical chemistry*, 89(5):3043–3050, 2017.

[79] Marie Doumeng, Lotfi Makhlouf, Florentin Berthet, Olivier Marsan, Karl Delbé, Jean Denape, and France Chabert. A comparative study of the crystallinity of polyetheretherketone by using density, dsc, xrd, and raman spectroscopy techniques. *Polymer Testing*, 93:106878, 2021.

[80] C Hedesiu, DE Demco, R Kleppinger, G Vanden Poel, W Gijsbers, B Blümich, K Remerie, and VM Litvinov. Effect of temperature and annealing on the phase composition, molecular mobility, and the thickness of domains in isotactic polypropylene studied by proton solid-state nmr, saxs, and dsc. *Macromolecules*, 40(11):3977–3989, 2007.

[81] Jing Zhao and Gregory B McKenna. Temperature divergence of the dynamics of a poly (vinyl acetate) glass: Dielectric vs. mechanical behaviors. *The Journal of chemical physics*, 136(15):154901, 2012.

[82] Sivasurender Chandran, Jorg Baschnagel, Daniele Cangialosi, Koji Fukao, Emmanouil Glynos, Liesbeth MC Janssen, Marcus Muller, Murugappan Muthukumar, Ullrich Steiner, Jun Xu, et al. Processing pathways decide polymer properties at the molecular level. *Macromolecules*, 52(19):7146–7156, 2019.

[83] Aya Samir, Fatma H Ashour, AA Abdel Hakim, and Mohamed Bassyouni. Recent advances in biodegradable polymers for sustainable applications. *npj Materials Degradation*, 6(1):68, 2022.